NUCLEAR ENGINEERING

MASSACHUSETTS INSTITUTE
OF TECHNOLOGY

Modeling of Fuel-To-Steel Heat Transfer in Core Disruptive Accidents

by

R. C. Smith, W. M. Rohsenow and M. S. Kazimi

MITNE 233

Department of Nuclear Engineering

Massachusetts Institute of Technology

June 1980

Modeling of Fuel-To-Steel Heat Transfer in Core Disruptive Accidents

by

R. C. Smith, W. M. Rohsenow and M. S. Kazimi

Report Issued Under Contract NRC-04-77-126

U.S. Nuclear Regulatory Commission

MODELING OF FUEL-TO-STEEL HEAT TRANSFER IN CORE DISRUPTIVE ACCIDENTS

ABSTRACT

A mathematical model for direct-contact boiling heat transfer between immiscible fluids was developed and tested experimentally. The model describes heat transfer from a hot fluid bath to an ensemble of droplets of a cooler fluid that boils as it passes through the hot fluid. The mathematical model is based on single bubble correlations for the heat transfer and a drift-flux model for the fluid dynamics. The model yields a volumetric heat transfer coefficient as a function of the initial diameter, velocity and volume fraction of the dispersed component. An experiment was constructed to boil cyclopentane droplets in water. The mathematical and experimental results agreed reasonably well.

The results were applied to investigate the possibility of steel vaporization during a hypothetical core disruptive accident in a liquid metal fast breeder reactor. The model predicts that substantial steel vaporization may occur in core disruptive accidents, if the steel reaches its saturation temperature rapidly enough. The potential importance of steel vaporization is dependent on the accident scenario.

ACKNOWLEDGEMENTS

The authors would like to thank Joseph "Tiny" Caloggero and Freddy Johnson for their help in constructing the apparatus for the experiment conducted in this work. In addition, thanks are due to Francis "Woody" Woodworth and the men of the Nuclear Engineering Department Machine Shop for their help with the experiment. The patient assistance of Gail Jacobson, Michele Halverson, Karen Stringi, and Wesley Fultz in preparing the final manuscript was most appreciated.

TABLE OF CONTENTS

TABLE OF CONTENTS (Cont'd)

LIST OF FIGURES

LIST OF FIGURES (Cont'd)

LIST OF TABLES

NOMENCLATURE

A	area
A_b	droplet surface area
A_p	projected area perpendicular to flow direction
B	parameter defined by Eq. (35)
C	δ_M/δ_m
C_D	drag coefficient
C_p	specific heat
D_o, D	initial and instantaneous equivalent spherical diameter
h_b	individual droplet heat transfer coefficient
h_v	volumetric heat transfer coefficient
H	constant defined by Eq. (33)
k	thermal conductivity
K_1, K_2	constants defined by Eqs. (83) and (84)
L_d	latent heat of vaporization of dispersed phase
m	$(1-x)(y+1)+1$
$\dot{m}_v$	mass flow rate
n	constant defined by Eq. (1) and Eq. (B-10)
n_b	number density of droplets
Nu	Nusselt number $\frac{h_b D}{k}$
∇p	pressure gradient
Pr	Prandtl number $\frac{\mu C_p}{k}$
r	equivalent spherical diameter ratio D/D_o
Re	Reynolds number $\frac{\rho U D}{\mu}$

NOMENCLATURE (Cont'd)

ΔT	temperature difference between continuous and dispersed phases
U_o, U, U_r	initial, instantaneous and relative droplet velocities; $Ur = (1-\alpha)^{n-1} U$
V	volume
$\dot{W}$	volumetric flow rate
z	axial displacement
α	void fraction (dispersed phase volume fraction defined by Eq. (25))
α_f	thermal diffusivity of fuel
β	angle defined by Figure 3
γ	constant defined by Eq. (20)
δ	liquid film thickness inside droplets
ρ	density
μ	viscosity

subscripts

a	onset of agglomeration values
b	droplet values
c	continuous phase properties
d	dispersed phase properties
dl	dispersed phase liquid
dv	dispersed phase vapor
f	fuel values
o	initial values
s	steel values
v	volumetric
max	maximum

NOMENCLATURE (Cont'd)

subscripts (Cont'd)

M	maximum
m	minimum

superscripts

x	exponent in Eq. (20)
y	exponent in Eq. (31)
w	exponent in Eq. (20)
m	$(1 - x)(y + 1) + 1$

1.0 INTRODUCTION

In safety analyses of liquid metal fast breeder reactors, hypothetical core disruptive accidents are usually considered. In the postulated unprotected loss-of-flow accident it is possible that the sequence of events will lead to a gradual melt-down of the core materials rather than an abrupt and energetic disassembly of the core. Presently it is impossible to predict the exact course such an accident will follow. On the basis of calculations performed at the Argonne National Laboratory [1], there is evidence to suggest that incoherency effects and other mitigating factors may limit reactivity insertion rates. If this is the case, there could be a more gradual transition from an essentially intact core geometry to the disrupted state, and for this reason the so-called "transition phase" of the accident has received considerable attention lately in fast reactor safety research. However, an analysis of this phase of the accident is extremely complicated because of the relatively long time frame and extensive material relocation involved. Currently, large computer codes to analyze hypothetical core disruptive accidents are being developed and tested in the United States and elsewhere. Perhaps the most significant contribution these codes have made to the investigation is the identification of the phenomena which are of primary importance in determining the accident energetics and the resulting containment requirements. In fact, as an integral part of the

developmental effort, researchers at the Los Alamos Scientific Laboratory conduct sensitivity studies with the SIMMER computer code [2] to identify the phenomena which require modeling improvements in the code. One mechanism that has been identified is heat transfer from hot molten fuel to cooler molten structural steel (see Figure 1). Since this mechanism could reduce the total vapor pressure generated by distributing the heat load over a large mass of material, it may be instrumental in mitigating the work potential of the expanding core. However, the effectiveness of this mechanism will strongly depend on the rate at which the heat is transferred.

Currently, the fluid dynamics modeling in the SIMMER code does not allow relative motion between different liquids. Consequently, fuel-to-steel heat transfer modeling is restricted to pure conduction, although a certain degree of flexibility is introduced by allowing variations in the conduction lengths. The purpose of this work was to investigate convective heat transfer during direct-contact evaporation in immiscible fluids and to compare the resulting convective heat transfer coefficients with conductive heat transfer coefficients to ascertain the magnitude and consequences of any discrepancies. Basically, the effort involved combining existing models for single bubble direct-contact evaporation with a drift-flux model to account for the influence the bubbles have on one another in a multibubble flow

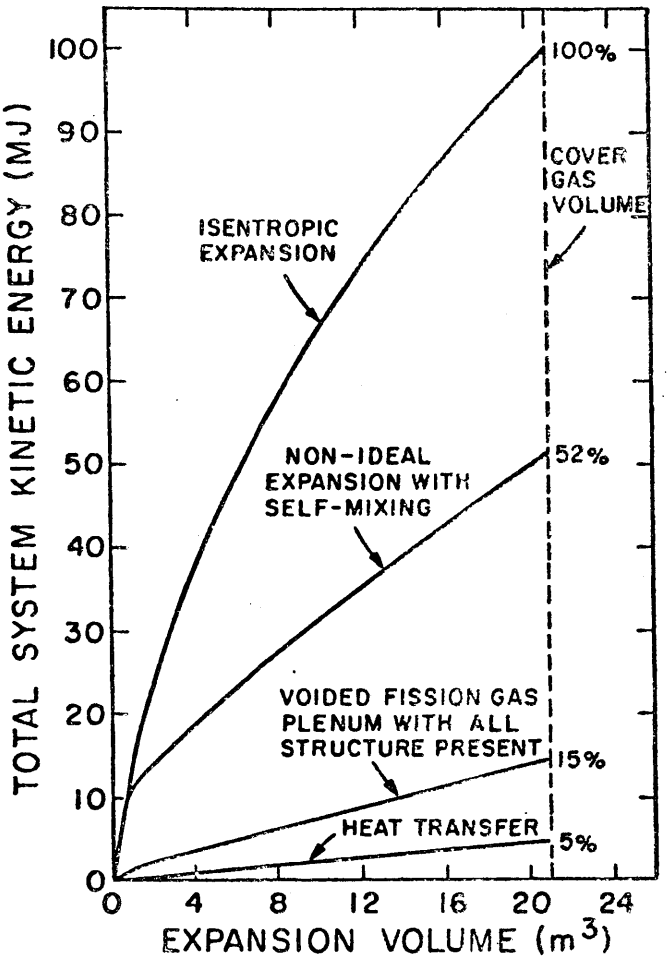

Figure 1. The Relative Importance of Various Phenomena in Predictions by SIMMER-I of the Kinetic Energy of Fluids Impacting on an LMFBR Vessel [21]

field. In addition, the resulting model was tested against experiments in which cyclopentane was vaporized by hot water in a direct-contact volume boiler similar to those used in earlier geothermal research.

2.0 THEORY

2.1 Description of the Problem

When saturated droplets of a fluid are allowed to percolate through a hotter and denser fluid with which it is immiscible, heat is transferred to the droplets and they will begin to boil. This mode of heat transfer is commonly referred to as direct-contact evaporation, and it is generally a very efficient means of heat transfer. For this reason the process has attracted a great deal of attention and there is currently much interest in using the process in projects ranging from geothermal heat extraction to sea water desalination.

Direct-contact evaporation is characterized by a rather indistinct and often variable heat transfer surface because the droplets grow, deform and sometimes oscillate as they evaporate. Consequently, quantification of the process by surface heat transfer coefficients becomes difficult and ambiguous. So it is more common to quantify the process in terms of volumetric heat transfer coefficients that depend on the mass flux and droplet size of the dispersed phase flowing through the continuous phase. Although many studies have been conducted to empirically determine volumetric heat transfer coefficients on a case by case basis, to the best of the author's knowledge this work represents the first attempt at analytically synthesizing a formula for volumetric heat transfer coefficients from "first principles", i.e. existing formulas for single bubble direct-contact

evaporation, bubble velocity correlations, the drift-flux model of two-phase flow and the principles of conservation of mass and energy. The problem then is to determine the behaviour of initially saturated liquid droplets as they flow through the hot continuous phase, and then to infer from their behavior a volumetric heat transfer coefficient as a function of the initial number density and droplet size and the displacement from their initial positions.

2.2 Droplet and Bubble Velocities

Throughout this work it is assumed that the relative velocity between the dispersed and continuous phases can be determined from the drift-flux model of two-phase flow which gives the relative velocity as [3].

$$U_r = (1 - \alpha)^{n-1} U \tag{1}$$

where U is the velocity of a single bubble in an infinite pool of the continuous component, α is the dispersed phase volume fraction and n is a parameter that depends primarily on α and usually varies from zero to three or four.

The velocity U of a single bubble is determined by solving a momentum equation which includes all of the important forces acting on the bubble. In general, pressure gradients and body forces such as gravity are opposed by drag and inertial forces

$$V(\tfrac{1}{2}\rho_c + \rho_d)\frac{dU}{dt} + A_p C_D \tfrac{1}{2}\rho_c U^2 = [\nabla p(1-\rho_d/\rho_c)]\ V \tag{2}$$

where V is the volume of the bubble, A_p is the projected area of the bubble in the direction of U, C_D is the drag coefficient and ρ_c and ρ_d are the densities of the continuous and dispersed components, respectively. For a two-phase droplet/bubble ρ_d is the volume weighted mean density, so that ρ_d decreases continuously for an evaporating droplet. The first term in Eq.(2) corresponds to the inertial force, and the first part of the first term represents the virtual mass of the displaced continuous component.[4] The second term represents the drag force, and the drag coefficient C_D includes the contributions of both form and shear drag. The third term represents the pressure gradient force. If there are no externally applied pressure gradients, then $\nabla p = g\rho_c$, and the right hand side of Eq. (2) becomes $Vg(\rho_c - \rho_d)$, which is just the buoyant force on the bubble.

The drag coefficient C_D depends on the characteristics of both the droplet/bubble and the flow, and there is no single formula for C_D which is applicable to all droplet/bubble sizes and shapes. It is customary to correlate C_D with the Reynolds's number, $Re_b = UD/\nu_c$, to derive empirical formulas for C_D for rigid spheres, liquid droplets, and gas bubbles.

For $Re_b < 2$, it is possible to solve the Navier-Stokes equations for flow around a solid sphere because the flow is laminar and sym-

metrical about the equator. The result is $C_D = 24/Re_b$ [5]. For a droplet/bubble, however, the situation is slightly different because of circulation of the fluid within the bubble caused by the finite dispersed component viscosity. The circulation allows a non zero surface velocity, so that C_D is less than that of a rigid sphere, and it also tends to retard the onset of boundary layer separation for the same reason. Consequently, the symmetrical laminar flow field prevails to higher values of Re_b than for a solid sphere, and

$$C_D = \left(24/Re_b\right) \frac{2\,\mu_c + 3\,\mu_d}{3\,\mu_c + 3\,\mu_d} \qquad (3)$$

for $Re_b < 4$. [6,7].

For $Re_b > 2$ the drag losses and the adverse pressure gradient around the back of a rigid sphere decelerate the fluid in the boundary layer and the streamlines begin to deform and curl up to form a toroidal vortex in the boundary layer near the rear stagnation point. Eventually backflow begins and boundary layer separation occurs around $Re_b = 17$. The separation point moves forward until Re_b=450 when the vortex ring reaches 108^o and breaks away from the sphere and vortex shedding into the wake begins [8,9]. This behavior persists and results in a fairly constant value of C_D= 0.44 until Re_b = 300,000 and the boundary layer suddenly becomes turbulent. Since a turbulent boundary layer

resists separation much better than a laminar one, the adverse pressure gradient associated with boundary layer separation disappears and C_D decreases suddenly.

For a droplet/bubble with $Re_b > 2$ the situation is complicated by the onset of droplet/bubble deformation associated with viscous drag and the hydrodynamic pressure. As Re_b increases these forces increase until they are comparable with the surface tension, and the droplet/bubble changes from a spherical to an ellipsoidal shape. Generally, the increase in projected surface area associated with the shape change more than compensates for the reduction in C_D associated with circulation, so that C_D is larger for a droplet/bubble than a rigid sphere [10]. In the neighborhood of $Re_b = 200$ to 800 the droplet/bubble begins to oscillate probably due to helical vortex shedding. There is some uncertainty as to whether or not the oscillations suppress internal circulation or merely cause eddy diffusion between the circulation streamlines, but in any case the onset of oscillations is associated with a sudden increase in C_D. Above $Re_b = 5000$ the hydrodynamic force dominates both viscous and surface forces so that gas bubbles change from an ellipsoidal to a spherical cap shape, while liquid droplets break up. For cap shaped bubbles several researchers have obtained the constant value of $C_D = 2.6$ [11,12,13].

The velocity of a droplet/bubble can be determined by substituting the appropriate formula for C_D into Eq. (2) and solving for U. Implicit in this analysis is the assumption that correlations for C_D obtained from isothermal, steady-state experiments are applicable to systems with significant droplet/bubble acceleration. The solution is obtained easily in the absence of droplet/bubble growth, since with a constant value of V and A_p Eq. (2) is a first-order ordinary differential equation with constant coefficients. Even if the droplet/bubble grows, it may be possible to solve Eq. (2) approximately, if the rate of growth is slow enough to justify neglecting the first term in the equation. However, if the droplet/bubble experiences rapid growth due to evaporation or expansion, the solution can become quite complicated since V and A_p become functions of time. In such cases information describing the bubble growth is required to solve Eq. (2) and a discussion of such cases is reserved for Appendix A where the velocity of rapidly evaporating droplets is considered. Here consideration is limited to droplet/bubbles with constant or slowly increasing values of V and A_p, so that the first term in Eq. (2) is negligible.

Neglecting the first term in Eq. (2) yields

$$U^2 = \frac{2V}{C_D A_p} \frac{\nabla p}{\rho_c}\left[1-\rho_d/\rho_c\right] \qquad (4)$$

Substituting $V = (\pi/6)D^3$, $A_p = (\pi/4)D^2$ and Eq.(3) in Eq.(4) yields

$$U = \left(\frac{1}{18}\right) \frac{3\mu_c + 3\mu_d}{2\mu_c + 3\mu_d} \frac{\nabla p}{\mu_c} \left(1 - \rho_d/\rho_c\right) D^2 \tag{5}$$

in the Stokes regime $Re_b < 2$. The velocity in the ellipsoidal regime can be determined in the same way using an expression for V/A_p appropriate for ellipsoidal bubbles. Levich advanced an argument based on balancing the hydrodynamic and surface forces to determine V/A_p.[14] Consider the simplified sketch in Figure 2. The hydrodynamic heat Δp exerts a force on the top of the bubble which tends to flatten the cylinder doing work:

$$W_{\Delta p} = -\Delta p(\pi r^2)\ \delta h \tag{6}$$

However, this force is opposed by the surface tension σ which acts to resist the increase in r:

$$W_\sigma = \sigma(2\pi r)\ \delta r \tag{7}$$

Since the bubble volume remains essentially constant:

$$\delta V = h\delta(\pi r^2) + (\pi r^2)\ \delta h = 0 \tag{8}$$

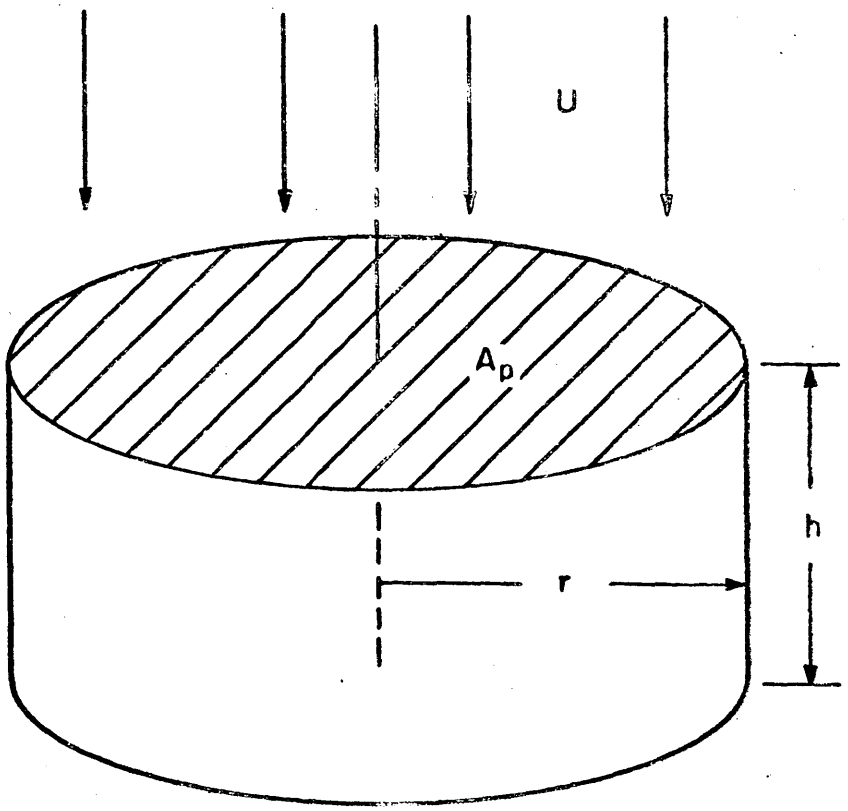

Figure 2. Levich's [14] Idealized Ellipsoidal Bubble

Substituting Eq.(7) into Eq.(5) yields:

$$W_{\Delta p} = -\Delta p(2\Pi r)\ h\delta r \tag{9}$$

and equating Eqs.(7) and (9) yields:

$$h = {}^{V}/_{A_p} = {}^{\sigma}/_{\Delta p} = \frac{2\sigma}{\rho_c U^2} \tag{10}$$

Therefore, Eq.(4) becomes:

$$U = \left(\frac{4\sigma\nabla p(1-{}^{\rho d}/_{\rho c})}{\rho_c{}^2 C_D}\right)^{1/4} \tag{11}$$

Which is independent of D. When the droplet/bubble changes from ellipsoidal to cap shaped, C_D assumes the constant value of 2.6 and Eq.(4) becomes

$$U = \left(\frac{4}{3}\ \frac{D}{2.6}\ \frac{\nabla p}{\rho_c}\ (1-{}^{\rho d}/_{\rho c})\right)^{1/2} \tag{12}$$

since $V = (\pi/6)D^3$ and $A_p = (\pi/4)D^2$ so that U is proportional to $\sqrt{D}$.

2.3 Single Bubble Heat Transfer Coefficients

Heat transfer to a single dispersed phase droplet evaporating in the continuous phase is a complicated process that depends on the fluid dynamics as well as the thermophysical properties of the two components. Despite recent extensive research into the subject, the theory has not yet advanced far enough to explain the observed behavior in quantitative detail. Current efforts are concentrated on understanding and modeling the fluid dynamics both inside and outside the droplet, since this determines thermal boundary layer thicknesses. However, a description of the fluid dynamics of an evaporating droplet is complicated by the fact that the evaporation changes both the dimensions and composition of the droplet. Hence, the characteristics of the flow can change drastically during the course of evaporation. Basically, the same considerations are fundamental to determining both the drag coefficient and the heat transfer coefficient, since the same phenomena are responsible for creating both the hydrodynamic and thermal boundary layers. Therefore,

hydrodynamic deformation, viscous shear, surface tension, internal circulation, vortex shedding and oscillation induced eddy diffusion are all of fundamental importance in describing both the external and internal flow configurations.

Since an evaporating droplet changes shape as it grows, it is customary to define an equivalent spherical diameter as

$$D = \left(\frac{6V}{\pi}\right)^{1/3} \tag{13}$$

Then the heat transfer coefficient is defined in terms of the surface area of the equivalent sphere

$$\dot{q} = h_b \, (\pi D^2) \, \Delta T \tag{14}$$

therefore, h_b must be formulated to correct for the difference between the actual droplet surface area and equivalent sphere surface area. Both the continuous and dispersed phases contribute to the overall thermal resistance, so that the heat transfer co-efficient is given by

$$\frac{1}{h_b} = \frac{1}{h_o} + \frac{1}{h_i} \tag{15}$$

where h_o and h_i are the heat transfer coefficients outside and inside the droplet, respectively. Depending upon the thermophysical properties and the disposition of the phases, the thermal resistance of one of the components may be negligible compared to the other.

Sideman and Taitel (15) assumed that the droplet could be represented by a sphere in a potential flow field, so they calculated the external heat transfer coefficient by solving the energy equation with a velocity profile determined from potential flow theory. Their result is

$$Nu_o = \left[\frac{3\text{Cos } \beta - \text{Cos}^3 \beta + 2}{\pi}\right]^{0.5} Pe_c^{0.5} \qquad (16)$$

where $\beta = \frac{1}{2}(360^o - \varepsilon)$ and ε is the opening angle of the liquid phase in the bubble (see Figure 3). They assumed that the thermal resistance of the dispersed phase was negligible and attempted to test their formula with data from a pentane-water experiment. (see Figure 5) Their formula did not work very well, however, for a number of probable reasons. During the early stages of evaporation the thermal resistance of the pentane in the droplet is probably significant. However, after only a small fraction of the pentane evaporates the droplet has grown enough to almost certainly justify ignoring the thermal resistance of the thin agitated film of pentane in the droplet. Far more questionable is the assumption that the flow around an expanding ellipsoidal or cap shaped droplet can be approximated by potential flow around a sphere.

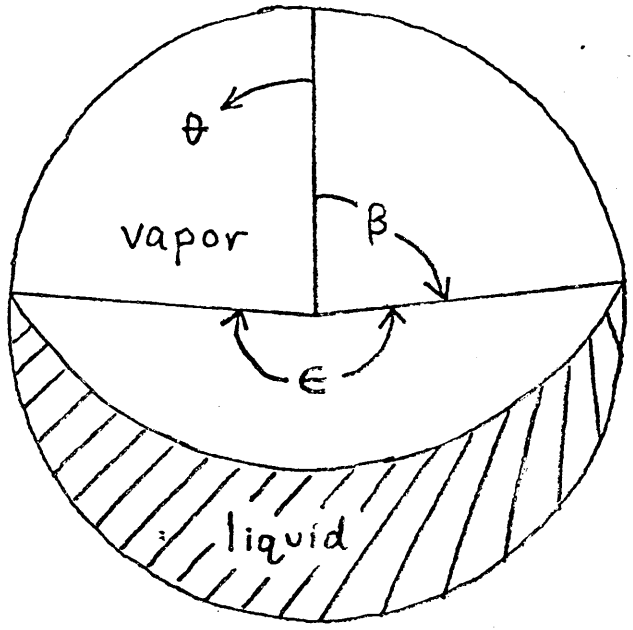

Figure 3. Sideman's Bubble Geometry [15]

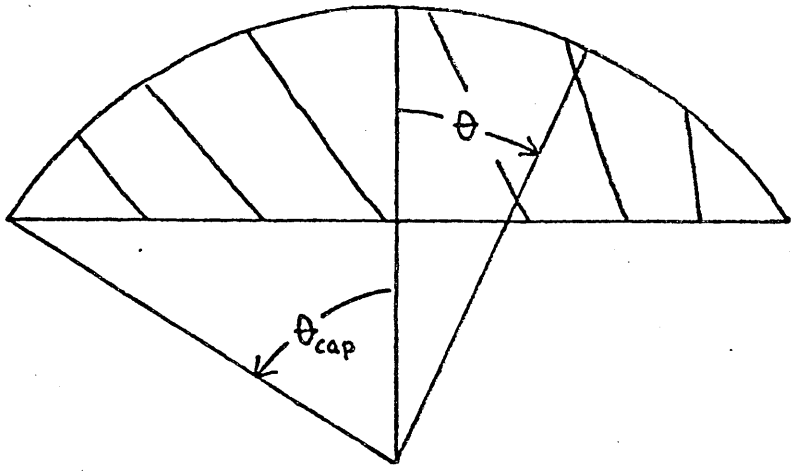

Figure 4. Nazir's Bubble Geometry [10]

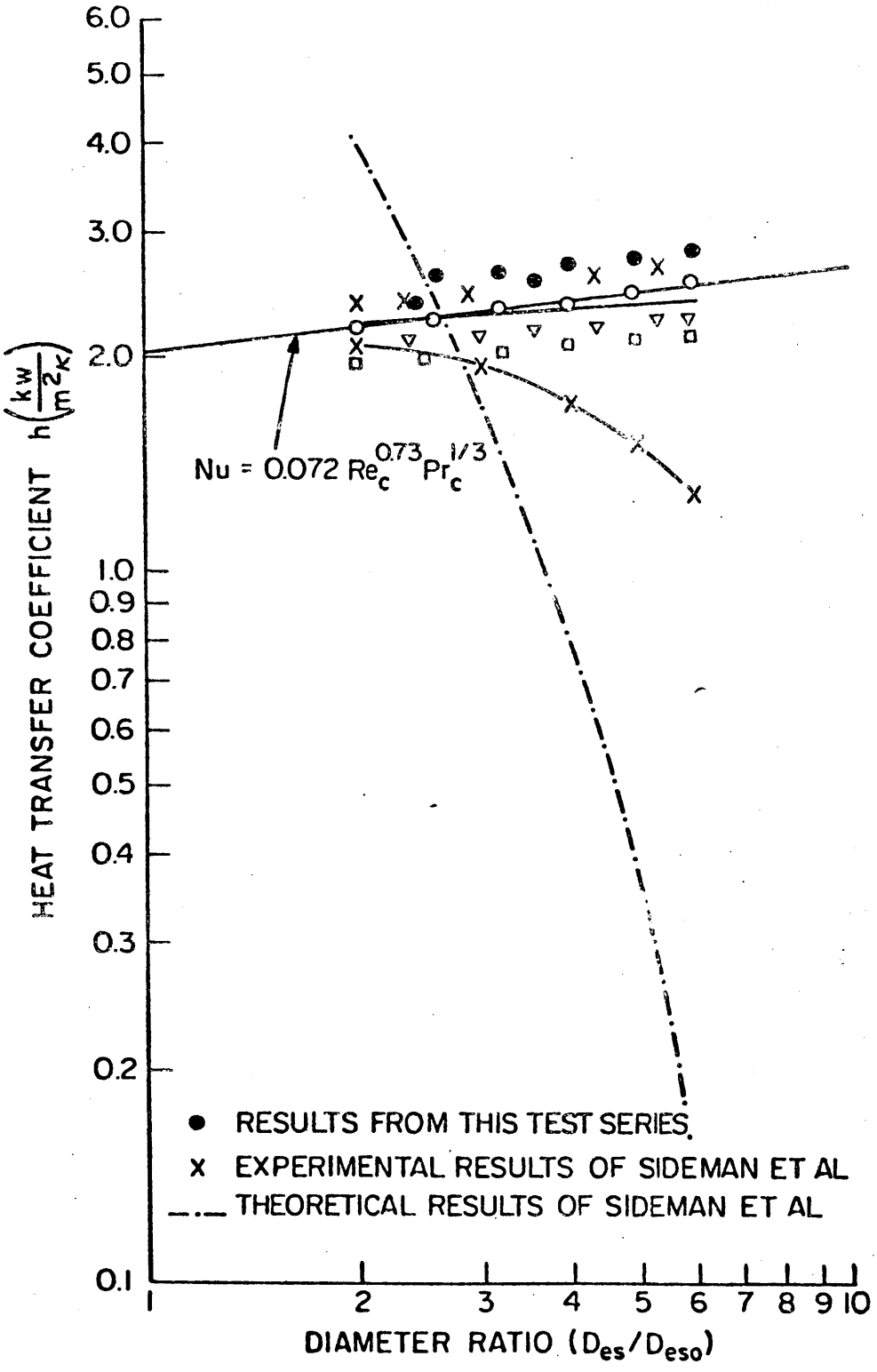

Figure 5. Nazir's Results [10] for Single Bubble Heat Transfer Using Butane and Water

Nazir [10] rejected the assumption that the thermal resistance of the dispersed phase liquid is negligible, so he developed a mathematical model to calculate the average thickness of the dispersed phase liquid film in the droplet as a function of the fraction evaporated. Basically, Nazir assumed the droplet is cap shaped (see Figure 4) and surrounded by a potential flow field in which Sideman's formula is valid. However, he postulated that oscillations of the droplet related to vortex shedding in the wake caused the unvaporized dispersed phase liquid to slosh around inside the droplet. Therefore, the entire interior surface of the bubble would be periodically coated with a thin film of dispersed phase liquid and zero would be the appropriate value of β in Sideman's equation, Eq (16). Sideman, on the other hand, had assumed that the liquid phase inside an evaporating droplet was confined to the lower portion of the droplet ($\beta \simeq 135°$) and that the $0<\theta<\beta$ (see Figure3) liquid-vapor interface was effectively adiabatic because of the low thermal conductivity of the vapor. Nazir then assumed that the film was accelerated by gravity and the sloshing motion, which is related to the Strouhal number, and he solved a simplified momentum equation for the film thickness by further assuming that the flow is laminar in the film.

His result is

$$Nu_f = K_1 \, (D/D_o)^{7/6} \qquad (17)$$

where D_o is the initial value of the equivalent spherical diameter before evaporation begins and K_1 is a constant for the butane-water system Nazir used.

Klipstein (16) conducted his research before Sideman or Nazir and did not attempt to derive an analytical model. Instead he made an extensive review of the available literature to identify potentially important phenomena for determining the heat transfer rate. He concluded that for his ethyl chloride - water experiment the thermal resistance of the dispersed ethyl chloride phase was negligible after only a few percent evaporation and that most of the heat transfer occurred through the turbulent wake. Therefore, he used regression analysis to successfully correlate his data with the following equation

$$Nu = 2 + .096\ Re_c^{0.93}\ Pr_c^{1/3} \qquad (18)$$

for the overall Nusselt number (see Figure 6). This is similar to the linear dependence on Re that was obtained for turbulent flow over cylinders, where the heat transfer also occurred primarily in the wake region. It is interesting to note that Nazir's data can be correlated by

$$Nu = 0.072\ Re_c^{0.73}\ Pr_c^{1/3} \qquad (19)$$

(see Figure 5) also, despite the fact that Eq. (17) implies that

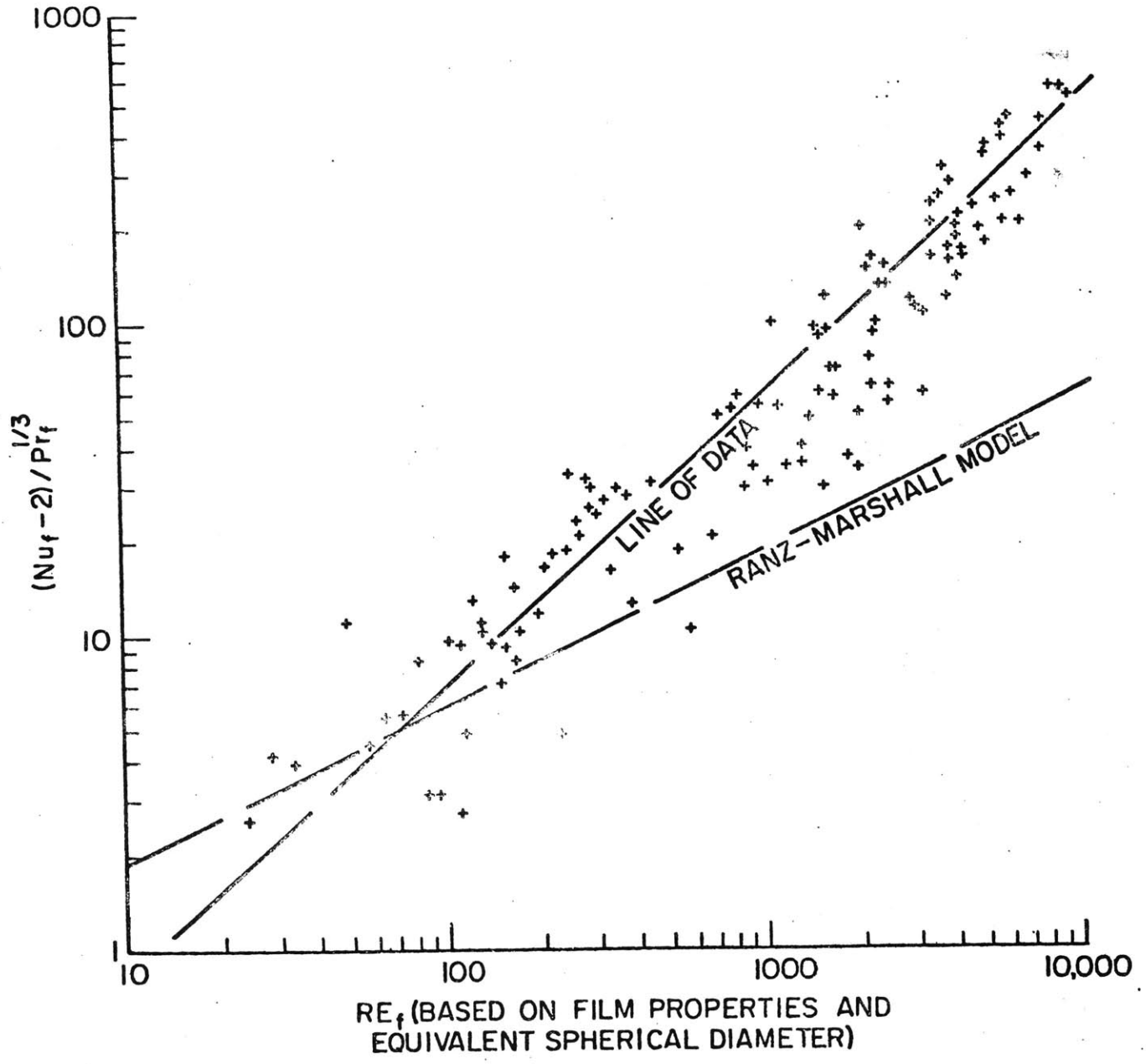

Figure 6. Klipstein's Results [16] for Single Bubble Heat Transfer in Direct Contact Boiler Using Ethyl Chloride and Glycerin-Water

the thermal resistance of the dispersed phase is controlling while Eq. (19) implies that it is negligible.

Because of the significant uncertainty concerning the details of direct-contact evaporation and because empirical correlations such as Eqs (18) and (19) successfully predict the trends of data from many experiments and reflect the dependence on Re_c characteristic of heat transfer in a turbulent wake, in this work the following simple formula will be used for calculating the single bubble heat transfer coefficient

$$Nu = \gamma Re^{x} Pr^{w} \qquad (20)$$

Refer to Appendix B for a more complete analysis of single bubble heat transfer coefficients and justification for the use of Eq (20).

Also, it is assumed in this work that vapor nucleation occurs when the droplet temperature reaches the saturation value. Although large degrees of superheating may be achieved in very pure liquids, in most practical applications there are sufficient impurities and other nucleation sites to preclude superheating.

2.4 Volumetric Heat Transfer Coefficients

Define the volumetric heat transfer coefficient as

$$h_v(z) = \frac{1}{z} \int_0^z A_b(z')\, n_b(z') h_b(z')\, dz' \qquad (21)$$

where z is the displacement from the point of origin $z=0$, where the droplets consist entirely of the liquid phase of the saturated dispersed

phase, and the remainder of the symbols are as defined below

A_b (z) ≡ surface area per bubble

n_b (z) ≡ number density of bubbles

h_b (z) ≡ overall heat transfer coefficient averaged over the bubble surface

Since it proves easier to express the quantities above in terms of the equivalent spherical diameter ratio of the bubbles, $r \equiv D/D_o$, rather than the displacement, the subsequent calculations are simplified considerably by changing the variable of integration as follows

$$h_v\,[z(r)] = [z(r)]^{-1} \int_{r_o}^{r} A_b(r')\, n_b\,(r')\, h_b\,(r')\, \frac{dz}{dr'}\, dr' \tag{22}$$

The problem then reduces to one of determining the relationship between the integrand and the equivalent spherical diameter ratio.

It simplifies matters to consider the problem in two parts -- analysis of the pre-agglomeration stage when bubbles may affect one another but retain their separate identities and analysis of the post-agglomeration stage when the volume fraction of space occupied by the bubbles becomes so large that they begin to coalesce as they collide in their passage through the continuous phase.

2.4.1 Pre-agglomeration Stage

The number density of bubbles in the pre-agglomeration stage is determined by requiring that the number flux of bubbles in the steady-state is conserved. Consider the sketch in Figure 7 Conservation of the number of bubbles demands that in the limit as $\Delta z \to 0$.

$$d/d_z\ (n_b\ U_r) = S \tag{23}$$

For the case of S = 0 (for example, no structural melting in CV) the solution of Eq. (23) is

$$n_b(r) = n_b(r_o)\ \frac{U_r\ (r_o)}{U_r\ (r)} \tag{24}$$

It also simplifies subsequent calculations to define a dispersed phase volume fraction by

$$\alpha(r) \equiv (\pi/6) D_o^3\ n_b(r)\ r^3 \tag{25}$$

The relationship between r and z can be determined by solving the following heat balance equation:

increase in vapor mass per bubble w.r.t. z	=	amount of heat transfer to bubble w.r.t. z divided by latent heat of vaporization of dispersed phase

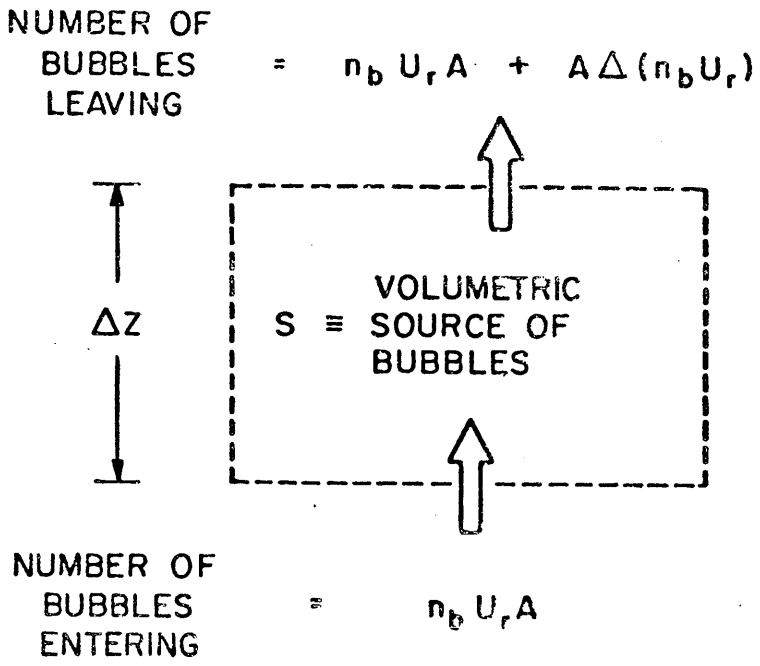

Figure 7. Diagram for the Pre-agglomeration Bubble Density Calculation

or in symbolic form

$$\frac{d}{dz}\left(\rho_{dv}\, V_{dv}\right) = \frac{1}{U_r}\frac{\dot{q}}{L_d} \tag{26}$$

The dispersed phase vapor volume per bubble is given by

$$V_{dv} = (\pi/6)\frac{\rho_{dl}\, D_o^3}{\rho_{dl} - \rho_{dv}}\left(r^3 - 1\right) \tag{27}$$

while the time rate of heat transfer per bubble is given by

$$\dot{q} = h_b(r)\, A_b(r)\, \Delta T \tag{28}$$

Substituting Eqs. (27) and (28) into Eq. (26) yields

$$(\pi/2)\frac{\rho_{dl}\, \rho_{dv}}{\rho_{dl} - \rho_{dv}} D_o^3\, r^2\, \frac{dr}{dz} = \frac{h_b\, A_b\, \Delta T}{U_r\, L_d} \tag{29}$$

When eqs. (24), (25) and (29) are combined with Eq. (22) the result is

$$h_v(r) = \frac{\alpha(r_o)}{z(r)}\, U_r(r_o)\, \frac{L_d}{\Delta T}\, \frac{\rho_{dl}\, \rho_{dv}}{\rho_{dl} - \rho_{dv}}\left(r^3 - 1\right) \tag{30}$$

To express z as a function of r it is necessary to integrate Eq. (29).

During the pre-agglomeration stage it is assumed that the droplets do not interfere significantly with one another; therefore,

n = 1 will be used in Eq. (1) during the pre-agglomeration stage, since this implies an "independent behavior" flow regime. Furthermore, the use of

$$U_r = U_o\, r^y \tag{31}$$

in Eq. (29) will demonstrate how the shape of the droplets affects the heat transfer coefficient, since y varies between zero and one half depending upon the shape of the droplet. Expressing Eq. (20) in terms of U_r and r yields

$$h_b = H\, U_r^x\, r^{x-1}\, D_o^{x-1} \tag{32}$$

where H is determined by the properties of the continuous phase

$$H = \gamma k_c\, Pr_c^w\, (\rho_c/\mu_c)^x \tag{33}$$

Substituting Eq. (31) and (32) into Eq. (29) yields

$$r^{(1-x)(y+1)}\, dr = B\, dz \tag{34}$$

where

$$B = 2\, \frac{h_{bo}\, \Delta T}{U_o\, D_o\, L_d}\, \frac{\rho_{dl} - \rho_{dv}}{\rho_{dl}\, \rho_{dv}} \tag{35}$$

Integrating Eq. (34) yields

$$\frac{r^{(1-x)(y+1)+1} - 1}{(1-x)(y+1) + 1} = Bz \tag{36}$$

Hence, Eq. (30) becomes

$$h_v(r) = 2\, m\, \alpha_o \frac{h_{bo}}{D_o} \frac{r^3 - 1}{r^m - 1} \tag{37}$$

where

$$m = (1-x)(y+1) + 1 \tag{38}$$

$$h_{bo} = H\, U_o^x\, D_o^{x-1} \tag{39}$$

or

$$h_v(z) = \frac{\alpha_o\, U_o\, L_d}{z\, \Delta T} \frac{\rho_{dl}\, \rho_{dv}}{\rho_{dl} - \rho_{dv}} \left[(1 + m\, B\, z)^{3/m} - 1\right] \tag{40}$$

which can also be expressed as

$$h_v(z) = 2\, m\, \alpha_o \frac{h_{bo}}{D_o} \frac{(1 + m\, B\, z)^{3/m} - 1}{m\, B\, z} \tag{41}$$

Notice that as a function of z, h_v depends on ΔT since B is directly proprotional to ΔT. For $(m\, B\, z) \gg 1$, $h_v(z)$ increases as $(\Delta T)^{(3-m)/m}$. This temperature dependence is not surprising since both A_b and h_b increse with r, and the average value of r within a given volume increases with ΔT due to increased evaporation. Thus, although the basic mechanism is convective in nature, the evaporative expansion results in a positive temperature dependence in $h_v(z)$.

Eq. (41) increases as m decreases and approaches the limiting value of

$$\lim_{m \to 1} \; h_v(z) = 2 \, \alpha_o \, \frac{k_{bo}}{D_o} \left[3 + 3(Bz) + (Bz)^2\right] \qquad (42)$$

Therefore, it appears that as the flow becomes more turbulent and $x \to 1$ in Eq. (20), the heat transfer coefficient is enhanced. Furthermore, as y increases in Eq. (31), the heat transfer coefficient decreases. This is not unexpected since the volume required for a given amount of heat transfer would tend to increase with the velocity.

2.4.2 Post-agglomeration Stage

From the pre-agglomeration analysis it is apparent that irrespective of the form of U_r the dispersed phase volume fraction α will grow as the bubbles grow. This situation will almost certainly result in the bubbles coalescing to some extent as their inter-collision frequency increases with α. However, it is uncertain to what extent the agglomeration will proceed. Consequently, the post-agglomeration stage of the model provides for this uncertainty by constraining the change in the dispersed phase volume fraction with respect to the displacement, $d\alpha/dz$, in the following manner

$$\frac{d\alpha}{dz} = \frac{d}{dz} \left(n_b (\pi/6) D^3\right) = f(D) \qquad (43)$$

where f(D) can be empirically determined from experimental data. There is evidence from both isothermal and pool boiling experiments [17, 18] suggesting that the void fraction increases only moderately following agglomeration, and Sideman and Gat [19] also concluded that the void fraction remained relatively constant following agglomeration in their direct-contact spray column evaporation. Sideman and Gat attributed this to flooding since the superficial velocity of the vapor was comparable to the values in air-water experiments at which flooding occurred. Therefore, there appears to be sufficient justification for assuming that α remains constant following agglomeration. To limit α to a maximum value of α_{max} while evaporation continues, it is necessary for the bubbles to accelerate. To satisfy this requirement n_b must decrease (through agglomeration) at such a rate that the larger bubbles created will have large enough velocities to "stretch out" the dispersed phase in the flow field enough to limit α to α_{max}. Mathematically, this requirement is equivalent to

$$\frac{d}{dz}\left(n_b(\pi/6)D^3\right) = 0 \quad \text{for} \quad z > z(\alpha_{max}) \tag{44}$$

where $z(\alpha_{max})$ is the position where $\alpha \to \alpha_{max}$ and agglomeration is assumed to commence. The solution of Eq. (44) is

$$n_b(D) = n_{ba}\,(D_a/D)^3 \qquad D > D_a \tag{45}$$

where the subscript a indicates that the quantity has the value it had at the onset of agglomeration.

Again, the problem reduces to determining how D varies with z; and, again, this can be analyzed by considering the conservation of energy. Therefore, consider the following simple sketch in Figure 8, where D_1 is the equivalent sperical diameter the bubble would have if the dispersed phase was all liquid and where $\dot{Q}_{c\to d}$, the rate of heat transfer to the dispersed phase from the continuous phase is given by

$$\dot{Q}_{c\to d} = h_b \ (\pi D^2) n_b \ \Delta T \ (A \ \Delta z) \tag{46}$$

A heat balance then gives

$$L_d \ \Delta \left[n_b \ U_r \ A(\pi/6) \ \frac{\rho_{dl} \ \rho_{dv}}{\rho_{dl} - \rho_{dv}} \ (D^3 - D_1^3) \right] = h_b (\pi \ D^2) n_b \ \Delta T \ (A \ \Delta Z)$$

or in the limit as $\Delta z \to 0$

$$d/dZ \left[n_b \ U_r \ (D^3 - D_1^3) \right] = 6 \ n_b \ h_b \ \frac{\rho_{dl} - \rho_{dv}}{\rho_{dl} \ \rho_{dv}} \ \frac{\Delta T}{L_d} \ D^2 \tag{47}$$

In Eq. (47) $n_b(D)$ is given by Eq. (45), and h_b is given by Eq. (32).

MASS OF VAPOR LEAVING PER UNIT TIME

$$= n_b U_r A \frac{\pi}{6} \frac{\rho_{dv}\rho_{dl}}{\rho_{dl}-\rho_{dv}} (D^3 - D_1^3) + A \frac{\pi}{6} \frac{\rho_{dv}\rho_{dl}}{\rho_{dl}-\rho_{dv}} \Delta\left[n_b U_r (D^3 - D_1^3)\right]$$

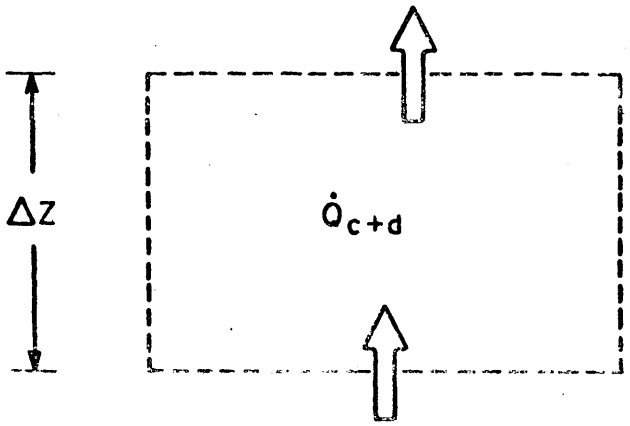

MASS OF VAPOR ENTERING PER UNIT TIME

$$= n_b U_r A \frac{\pi}{6} \frac{\rho_{dv}\rho_{dl}}{\rho_{dl}-\rho_{dv}} (D^3 - D_1^3)$$

Figure 8. Diagram for the Post-agglomeration Energy Balance Calculation

During the post-agglomeration stage it is assumed that the flow is churn-turbulent, since there is experimental evidence that cap shaped bubbles will accelerate in the wake of their predecessors since they encounter reduced drag there. To account for this 'drafting' behavior n=0 is used in Eq(1) during the post-agglomeration stage, so that U_r tends to increase with α. However, since it is also assumed that α is limited to α_{max}. Eq(1) becomes

$$U_r = (1-\alpha_{max})^{-1} U_o (D/D_o)^{y_a} \tag{48}$$

Because of agglomeration, D_1, the diameter the droplet would have if the dispersed phase was all liquid, is now a function of z. Consequently, it is necessary to determine the relationship between D_1 and D before Eq(47) can be solved. The desired relationship is derived by invoking the principle of conservation of dispersed phase mass flux

$$\rho_{d1}(\pi/6)D_1^3 n_b(D) U_r(D) = \rho_{d1}(\pi/6)D_o^3 n_{ba} U_{ra} \tag{49}$$

which can be solved for D_1 to yield

$$D_1^3 = \frac{n_{ba}}{n_b(D)} \frac{U_{ra}}{U_r(D)} D_o^3 \tag{50}$$

or if Eq(45) is substituted for $n_b(D)$

$$D_1^3 = \frac{U_{ra}}{U_r(D)} \left(\frac{D_o}{D_a}\right)^3 D^3 \tag{51}$$

Substituting Eqs(45) and (50) into Eq (47) and simplifying the result yields

$$\frac{d}{dz}\left[U_r(D)-U_{ra}(D_o/D_a)^3\right] = 6\left[\frac{\rho_{dl}-\rho_{dv}}{\rho_{dl}\ \rho_{dv}}\right]\frac{h_b\Delta T}{D\ L_d} \tag{52}$$

or since the second term in the derivative is constant

$$\frac{d}{dz}\ U_r(D) = 6\left[\frac{\rho_{dl}-\rho_{dv}}{\rho_{dl}\ \rho_{dv}}\right]\frac{h_b\Delta T}{D\ L_d} \tag{53}$$

Substituting Eq(48) into Eq(53) yields

$$(D/D_o)^{y_a}\frac{d}{dz}(D/D_o) = \frac{6}{y_a}\frac{(1-\alpha_{max})}{U_o D_o L_d}\left[\frac{\rho_{dl}-\rho_{dv}}{\rho_{dl}\ \rho_{dv}}\right] h_b\Delta T \tag{54}$$

Substituting Eq (48) into Eq(32) yields

$$h_b = H\left[\frac{U_o(D/D_o)^{y_a}}{1-\alpha_{max}}\right]^{x_a} D^{x-1} \tag{55}$$

and substituting Eq(55) into Eq(54) yields

$$(D/D_o)^{m_a-1}\frac{d}{dz}(D/D_o) = \frac{6}{y_a}(1-\alpha_{max})^{1-x_a}\left[\frac{\rho_{dl}-\rho_{dv}}{\rho_{dl}\ \rho_{dv}}\right]\frac{h_{bo}\Delta T}{U_o D_o L_d} \tag{56}$$

Integrating Eq(56) yields

$$\frac{1}{m_a}\left[(D/D_o)^{m_a}-(D_a/D_o)^{m_a}\right] = \frac{6}{y_a}(1-\alpha_{max})^{1-x_a}\left[\frac{\rho_{dl}-\rho_{dv}}{\rho_{dl}\ \rho_{dv}}\right]\frac{h_{bo}\Delta T}{U_o D_o L_d}(z-z_a) \tag{57}$$

During the post-agglomeration stage Eq(22) assumes the form

$$h_v = \frac{1}{z_a+(z-z_a)}\left\{ \int_{D_o}^{D_a} A_b n_b h_b \left(\frac{dz}{dD}\right) dD + \int_{D_a}^{D} A_b n_b h_b \left(\frac{dz}{dD}\right) dD \right. \tag{58}$$

The first integral in Eq(58) was evaluated in the pre-agglomeration stage

$$\int_{D_o}^{D_a} A_b n_b h_b \left(\frac{dz}{dD}\right) dD = \alpha_o U_o \frac{L_d}{\Delta T} \left(\frac{\rho_{dl}\ \rho_{dv}}{\rho_{dl}-\rho_{dv}}\right) (r_a^3-1) \tag{59}$$

The second integral in Eq(58) is evaluated similarly with the use of Eqs(45) and (54)

$$\int_{D_a}^{D} A_b n_b h_b \left(\frac{dz}{dD}\right) dD = \frac{\alpha_{max} U_o}{1-\alpha_{max}} \frac{L_d}{\Delta T} \left(\frac{\rho_{dl}\ \rho_{dv}}{\rho_{dl}-\rho_{dv}}\right) (r^{y_a}-r_a^{y_a}) \tag{60}$$

Finally, substituting Eq(36) for z_a and Eq(57) for $(z-z_a)$ into Eq(58) yields

$$h_v(r) = 2\frac{h_{bo}}{D_o} \frac{\alpha_o(r_a^3-1) + \frac{\alpha_{max}}{1-\alpha_{max}} (r^{y_a}-r_a^{y_a})}{\frac{1}{m_o}(r_a^{m_o}-1) + \frac{y_a}{3m_a}(1-\alpha_{max})^{x_a-1}(r^{m_a}-r_a^{m_a})} \tag{61}$$

From Eq(51) it is obvious that y_a must be greater than zero (i.e. U_r increases with D) if D/D_1 increases (i.e. evaporation continues). As a function of z, Eq(61) can be written

$$h_v(z) = \frac{2h_{bo}}{D_o Bz} \left[\alpha_o\{(1+m_o Bz_a)^{3/m_o}-1\} + \frac{\alpha_{max}}{1-\alpha_{max}}\right.$$

$$\left.\cdot\{(1+m_a Bz_a + {}^{3}/_{y_a}(1-\alpha_{max})^{1-x_a} m_a B(z-z_a))^{y_a/m_a} - (1+m_a Bz_a)^{y_a/m_a}\}\right] \tag{62}$$

To use Eq. (62) it is necessary to determine the initial values of the droplet diameter and velocity, D_o and U_o, the dispersed phase volume fraction, α_o, and the single droplet heat transfer coefficient h_{bo}. The user must also specify values for x_a, y_a, m_o and α_{max}. h_{bo} can be calculated from Eqs. (33) and (39) after values of D_o and U_o have been obtained and x has been specified. Eq. (62) was derived assuming the values of x during the pre-agglomeration and post-agglomeration stages are equal. If experimental evidence suggests that the Re dependence of Nu changes following the onset of agglomeration, it will be necessary to rederive Eq. (62) using different values of x during the pre-agglomeration and post-agglomeration stages. The values of y before and after agglomeration are not necessarily assumed to be equal, but y_z must be greater than zero to provide the mechanism for limiting α to α_{max}. M_o is calculated from Eq. (38) using the pre-agglomeration value of y and x. The specification of α_{max} is left to the discretion of the user. However, if the value of α_{max} that correlates the heat transfer data does not correlate the void fraction data, there will be serious doubts concerning the validity of the model.

3.0 EXPERIMENT

3.1 Introduction

In order to test the validity of the mathematical model developed and described in the preceding text, an experiment was designed and conducted. The design underwent extensive modifications during the course of this work as a result of both safety considerations and operational difficulties.

Originally, the volumetric heat transfer coefficient for two immiscible fluids was to have been measured directly for comparison with the predictions of the model. The intent was to measure the condensation rate of a fluid which had evaporated while rising through a pool of the hotter and denser fluid. Then, assuming only the latent heat of vaporization L_d had been transferred, the volumetric heat transfer coefficient would be given by

$$h_v = \frac{L_d \dot{m}_v}{V \Delta T} \tag{63}$$

where $\dot{m}_v$ is the condensation mass flow rate, V is the reaction volume and ΔT is the difference between the temperature of the hot continuous component and the saturation temperature of the dispersed component.

Unfortunately, all of the fluids suitable for use as the dispersed phase were flammable, and restrictions were placed on their use. Specifically, the limitations placed on acceptable

flow rates resulted in a decision to operate the experiment at lower dispersed phase injection rates than originally intended. It was also concluded that data interpretation would be too complicated with incomplete evaporation because it would be difficult to account for the effect of bulk boiling in the layer of dispersed phase liquid that would form on top of the continuous phase.

With complete vaporization, $\dot{m}_v$ in Eq. (63) is equal to the dispersed phase injection rate, a quantity which is relatively easy to measure. Therefore, to calculate h_v from Eq. (63), it is only necessary to measure V, the minimum volume required for complete evaporation. For a reaction vessel with a constant cross-sectional area, it is only necessary to measure the depth of the continuous phase required for complete evaporation.

According to the remarks following Eq. (62), the model includes a constraint on the maximum value of the void fraction to account for the effect of agglomeration. Since the model does not prescribe a method for calculating α_{max}, the user is free to specify any value of α_{max} in Eq. (62). However, if the value of α_{max} that correlates the heat transfer data in an experiment does not also approximately correlate the void fraction data, then there is no reason to believe that the model is physically accurate or that it has any use as an analytical tool. Consequently, as part of the verification procedure, the average void fraction was measured for comparison with the average values calculated using the values of α_{max} that correlated the heat transfer data.

Because the model developed in Section 2.0 requires the initial values of the droplet diameter and velocity, an auxillary experiment was conducted by Bordley [20] to photographically determine these values. Using the apparatus assembled for this work and a high speed motion picture camera, Bordley obtained photographs of Freon TF droplets evaporating in water.

3.2 The Selection of Materials

Careful consideration was given to the selection of the materials for the experiment. In addition to being immiscible, the fluids were selected on the basis of their relative densities, saturation temperatures, Prandtl numbers and their price. After an extensive search through tables of thermophysical properties, it was concluded that an organic liquid in water was the best choice. Cyclopentane was selected because its density and Prandtl number relative to water approximated a stainless steel-UO_2 system and because its saturation temperature of $49.6^{o}C$ precludes boiling at room temperature yet is low enough to allow relatively large values of ΔT in hot water. The relevant thermophysical properties of cyclopentane and water are listed in Table 1.

Because cyclopentane is highly flammable, it was necessary to construct the experiment to ensure that the integrity of the system would not be jeopardized by any reasonable incident. Consequently, the cyclopentane pump was explosion-proof, the piping

TABLE 1

THE THERMOPHYSICAL PROPERTIES OF CYCLOPENTANE AND WATER

	Property	Units	Cyclopentane	Water
Liquid Density	ρ_l	gm/cm^3	0.668	1.0
Vapor Density	ρ_v	gm/cm^3	.00309	
Liquid Viscosity	μ	gm/cm sec	.00322	.00517
Liquid Thermal Conductivity	k	cal/sec °C	.000301	.00154
Liquid Specific Heat	C_p	cal/gm C	.3113	1.0
Latent Heat of Vaporization	L_d	cal/gm	100	
Liquid Prandtl Number	Pr		3.33	3.36

was all copper and the thick-walled glass reaction vessel was enclosed in a hood with several fire extinguishers nearby.

3.3 Description of the Experiment

The experiment, which is depicted schematically in Figure 9, consisted essentially of a three-phase direct-contact heat exchanger and condenser in a closed loop arrangement.

The cycle commenced with pump P_1 drawing cyclopentane from the cyclopentane storage vessel (CSV) and injecting it into the lower cylinder of the reaction vessel (RV). The cyclopentane flow rate was monitored by a Fischer & Porter rotameter F_1 and adjusted with valves V_1 and V_2. V_1 admitted the cyclopentane to the reaction vessel, while V_2 discharged the surplus flow back into the cyclopentane storage vessel. The two ball type valves were required to regulate the flow because the Viking rotary gear pump displaced a constant volume of cyclopentane.

The reaction vessel (see Figure 10) consisted of two glass cylinders separated by a perforated 3/8" Lexan distribution plate. The Dow Corning glass cylinders were both 225 mm in diameter, but the lower one had a length of 200 mm while the upper one was 300 mm long. The perforated plate was bolted between the flanges holding the cylinders together, and asbestos gaskets were used on both sides of the plate to prevent leakage. 1/4" Lexan plates and asbestos gaskets were also used to seal the top and bottom of the vessel. Threaded penetrations were drilled into the Lexan

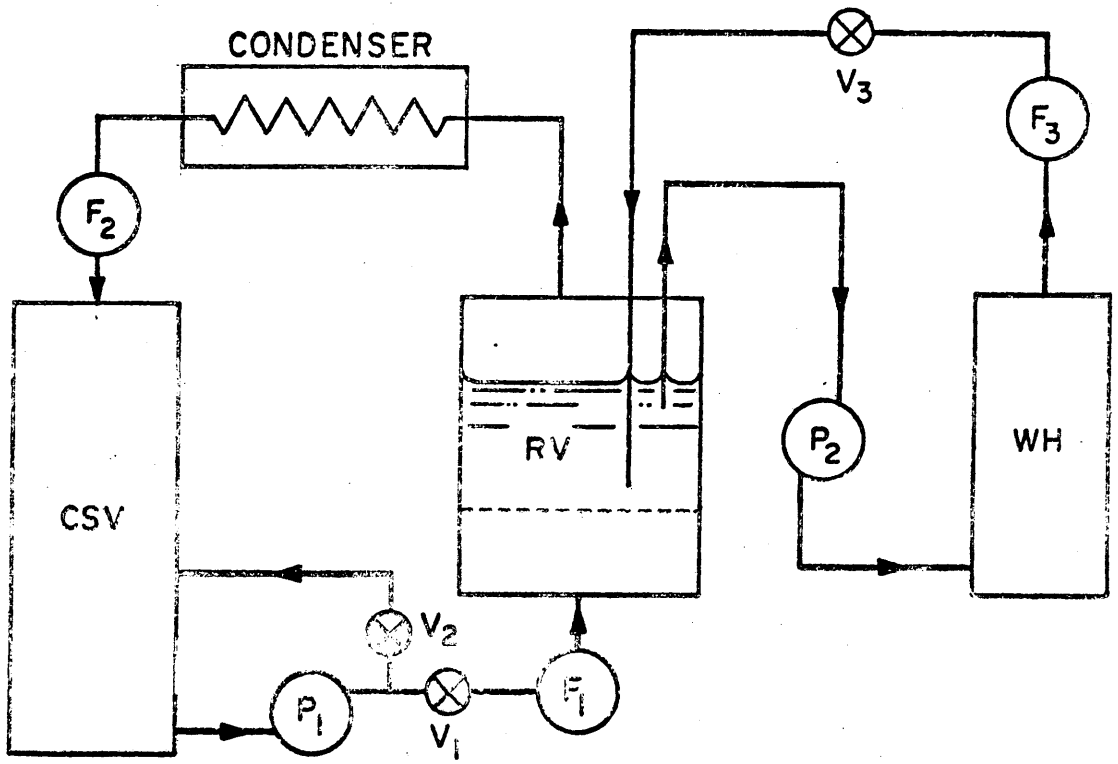

Figure 9. Schematic of the Apparatus used in the Cyclopentane-Water Experiment

CSV:	Cyclopentane Storage Vessel	P:	Pump
RV:	Reaction Vessel	V:	Valve
WH:	Water Heater	F:	Flow Meter

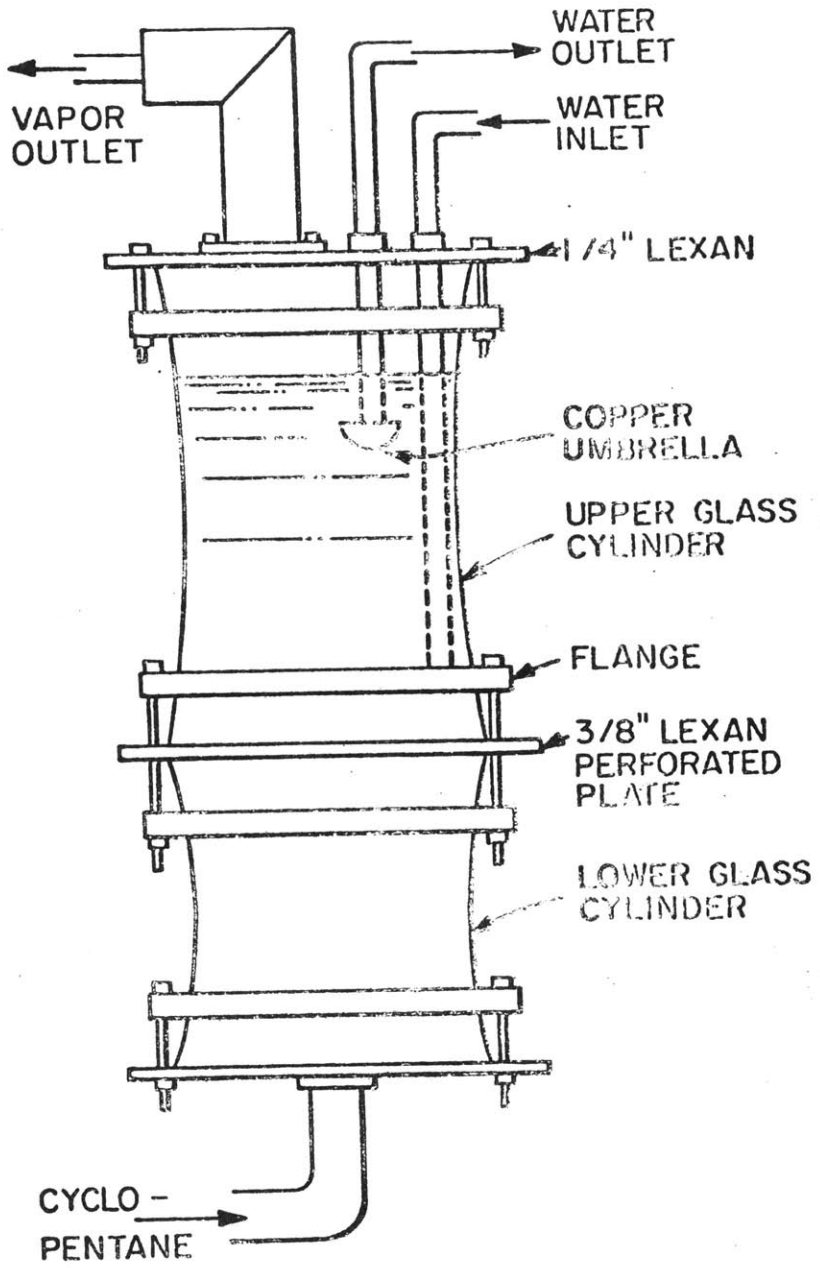

Figure 10. The Reaction Vessel

plates so that the copper tubing used could be secured with compression fittings.

Cyclopentane from the lower cylinder percolated through the 0.5 mm diameter holes in the distribution plate into hot water in the upper cylinder. Thermal conduction through the distribution plate caused modest surface boiling of the cyclopentane in the lower cylinder, so that it can be assumed that the cyclopentane droplets were at their saturation temperature upon contacting the hot water in the upper cylinder. At low flow rates, the cyclopentane tended to nucleate prior to detaching from the holes as discrete two-phase droplets. However, at low values of ΔT, less than $7^{o}C$, a significant fraction of the droplets failed to nucleate during their ascent. The size of the droplets at detachment tended to decrease with increasing ΔT, probably because the buoyant force overcame the force of surface tension sooner as the rate of evaporation increased. At higher flow rates the cyclopentane jetted through the holes and nucleated as the jets broke up. In fact, nucleation appeared to be responsible for the break-up of the jets, since the break-up was delayed considerably when the jets failed to nucleate.

Careful observation revealed that the vapor collected in the dome of the two-phase droplets during the early stages of evaporation. As evaporation continued and the droplets rose, it became increasingly difficult to distinguish the two phases within the droplets because the liquid occupied such a small volume.

It is probable that the liquid formed a film around the bottom of the droplet because no separation of the vapor from the liquid droplet was observed. However, the extent of liquid film spreading in the droplet could not be determined due to the thin nature of the film and the presence of droplet oscillations that hindered visual observations. Nonetheless, it was easy to identify the transition from spherical to ellipsoidal to cap-shaped droplets.

Cyclopentane vapor left the reaction vessel through a chimney and was condensed in a shell and tube type heat exchanger cooled by cold tap water. To increase precision, the flowmeter F_2 was replaced by a graduated cylinder in which the condensed cyclopentane was collected before being dumped back into the cyclopentane storage vessel. In steady-state operation all of the cyclopentane was vaporized, and the flow rate of F_1 was compared to the rate of collection in the graduated cylinder to check for equality.

The hot water in the upper cylinder was circulated in a separate closed loop consisting of a thermostatically controlled 18 kW Chromalox electric water heater (WH), a Bell & Gossett circulation pump (P_2), and rotameter (F_3) and the reaction vessel. The hot water entered the upper cylinder of the reaction vessel about 4 cm above the distribution plate through a hoop shaped sparger constructed from 1/2" copper tubing. A series of sixty-four holes with diameters varying from 0.16" to 0.50" were drilled in the bottom of the hoop to ensure a circumfrentially uniform

flow distribution. The hot water flowed cocurrently upward with the cyclopentane droplets and exited the reaction vessel through a 5/8" suction line connected to the pump. Isolating the inlet of the suction line from the cyclopentane droplets proved to be the major obstacle to the proper operation of this experiment. Initially, the end of the suction line was unmodified, but even at modest cyclopentane flow rates vapor entered the line and restricted circulation of the water. Next an umbrella fashioned from hammered copper was soldered to the tube to divert the cyclopentane droplets, but even this proved unsuccessful as the cyclopentane flow was increased. Finally, a sheet of thin aluminum was constructed to separate the suction line from the mainstream of the flow, and this solved the problem. The valve V_3 and rotameter F_3 were used to regulate and monitor the flow of water, respectively.

Instrumentation for the experiment consisted of thermocouples in addition to the two rotameters and the graduated cylinder. The 12" long Type E Chromel-Constantan Omega thermocouples had four second time constants. Preliminary tests with five thermocouples positioned at different axial levels in the upper cylinder indicated there was no significant axial temperature gradient. The absence of a temperature gradient and the observation of small, rapid temperature fluctuations imply that there was considerable mixing in the water. In subsequent experiments only one thermocouple could be inserted far enough into the vessel to measure the temperature because the water depth had to be decreased to yield the necessary data. However, because the temperature

measurements did not change significantly when the experiments were repeated, the measurements are reliable. The output from the thermocouples was monitored by an electronic Kaye Data Logger with an LED display and data printer. The temperature of any thermocouple could be displayed instantaneously, and the data from the channels could be printed on command or periodically (the maximum logging rate was limited to one per minute).

3.4 Operation of the Experiment

The experiment was conducted as follows:

The thermocouple plug was removed to fill the upper cylinder with clean tap water and to introduce a siphon hose to a drain. P_2 was started to circulate the water, as verified by F_3, while the siphon operated to remove any gross impurities from the system. When the water appeared clear, the siphon hose was removed. The thermocouples were reinserted and WH was set to the desired water temperature. After the designated temperature was reached, P_2 and WH were shut off, the thermocouple plug was again removed and the siphon line was reintroduced to lower the water level to the desired depth. Then the siphon was removed and the thermocouples reinserted.

Next, cold tap water was circulated through the cyclopentane condenser, V_1 was closed, V_2 was opened and P_1 was activated. V_1 and V_2 were then slowly adjusted to achieve the desired cyclopentane injection rate as measured by F_1. The temperature decline of the water was measured by F_1. The temperature decline of the water was measured

until the appearance of a layer of cyclopentane on top of the water indicated that vaporization of the cyclopentane was incomplete. The values of the water depth before and after swell, the cyclopentane injection rate and water temperature at the start of incomplete vaporization were finally recorded, and the run was complete. The experiment was repeated for several values of the water depth and the cyclopentane injection rate.

3.5 Results of the Experiment

Two series of experiments were conducted. The first series was conducted to establish the proper values of the constants in the formula for the heat transfer coefficient of a single droplet, Eq. (20). The second series was conducted to examine the effect of large void fractions and bubble agglomeration on the volumetric heat transfer coefficient.

In the first series of experiments, cyclopentane was injected at a constant flow rate of 6.31 cm^3/sec into the hot water through seven 0.5 mm diameter holes arranged in a hexagonal array with a 5.0 cm pitch. The minimum water temperature required to vaporize the cyclopentane completely was measured as a function of the water depth. The large pitch was selected intentionally to minimize the influence the bubbles would have on one another, so that this series of experiments could be used to ascertain the proper values of the constants in the formula for the heat transfer coefficient for single bubbles. The measured values of water temperature required for complete evaporation

in this series of experiments are presented in Figure 11. The data and associated error bars bound the results of two independent runs.

In the second series of experiments, cyclopentane was injected into the hot water through nineteen 0.5 mm diameter holes arranged in a hexagonal array with a 2.9 cm pitch. Again, the minimum water temperature necessary for complete evaporation was determined as the water depth was varied. The smaller pitch and larger number of holes used in this series of experiments resulted in larger void fractions and substantial agglomeration compared to the first series of experiments. The measured values of water temperature required for complete evaporation in this series of experiments are presented in Figure 12. The measured values of the average void fraction (determined according to Eq. (73)) in this series of experiments are presented in Figure 13. Again, the data and associated error bars bound the results of two independent runs. The dashed line in Figure 13 was drawn to correlate the data linearly, since the average void fraction usually displays a linear relationship to the dispersed phase superficial velocity below the flooding condition.

The error bars on the data represent the author's estimation of the error that results for the following reasons. Although the system contained impurities, droplet nucleation was delayed or absent in a significant fraction of the droplets as the temperature difference decreased. Below 7 ^{o}C evaporation was incomplete irrespective of water depth; hence, this value of the temperature difference appears to represent the minimum superheat requirement

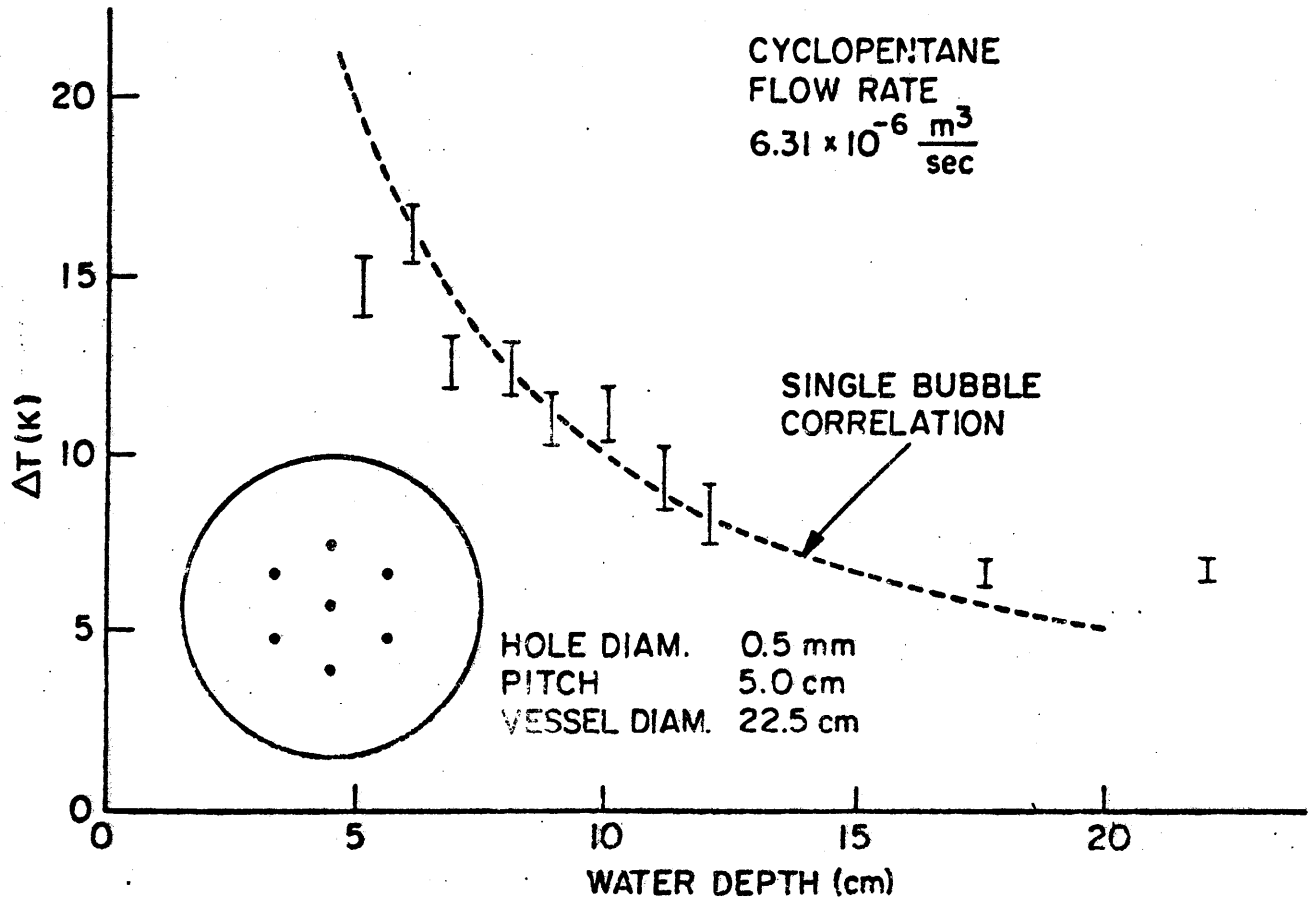

Figure 11. Minimum Water Temperature Superheat above Cyclopentane Saturation Temperature (49.7 °C) as a Function of Water Depth without Agglomeration

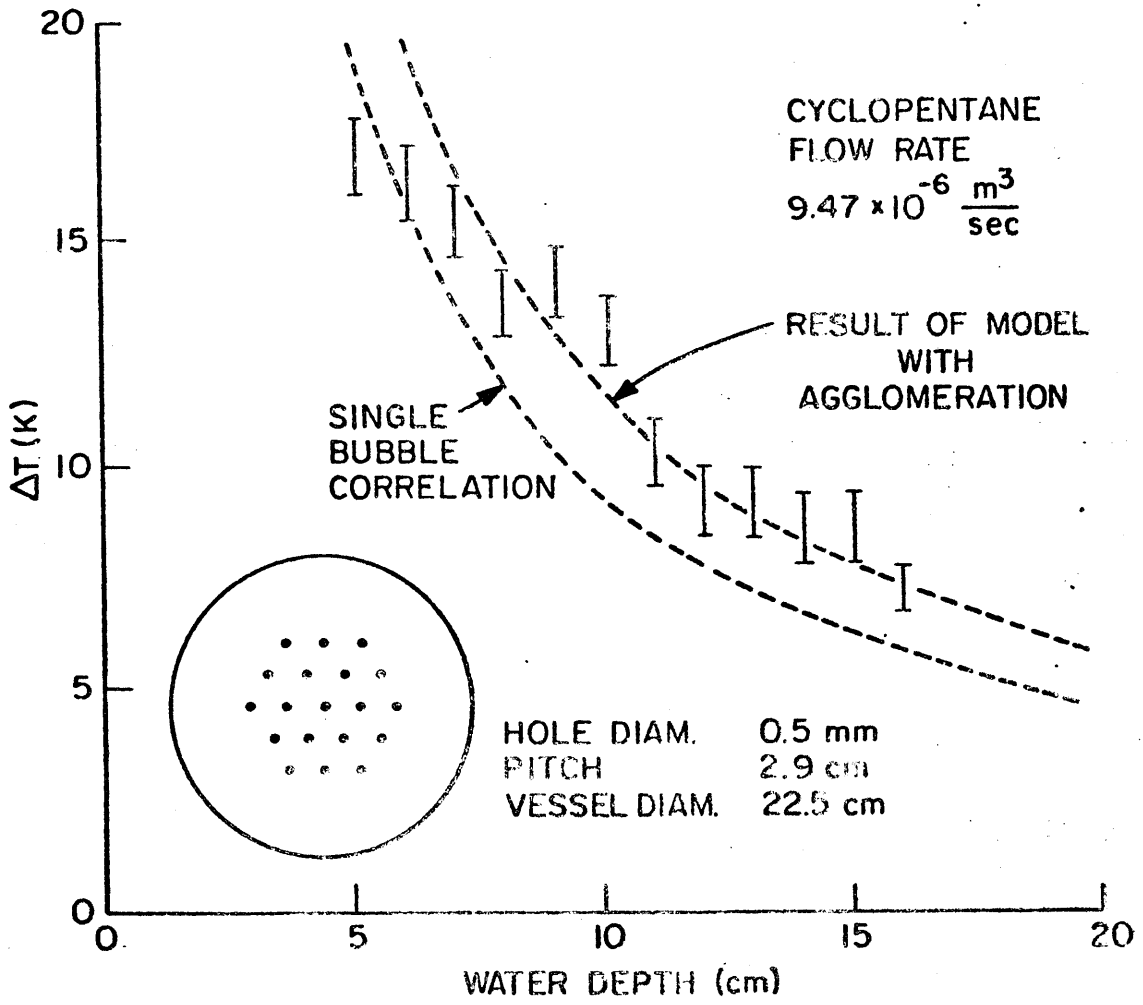

Figure 12. ΔT_{min} vs. Water Depth With Agglomeration

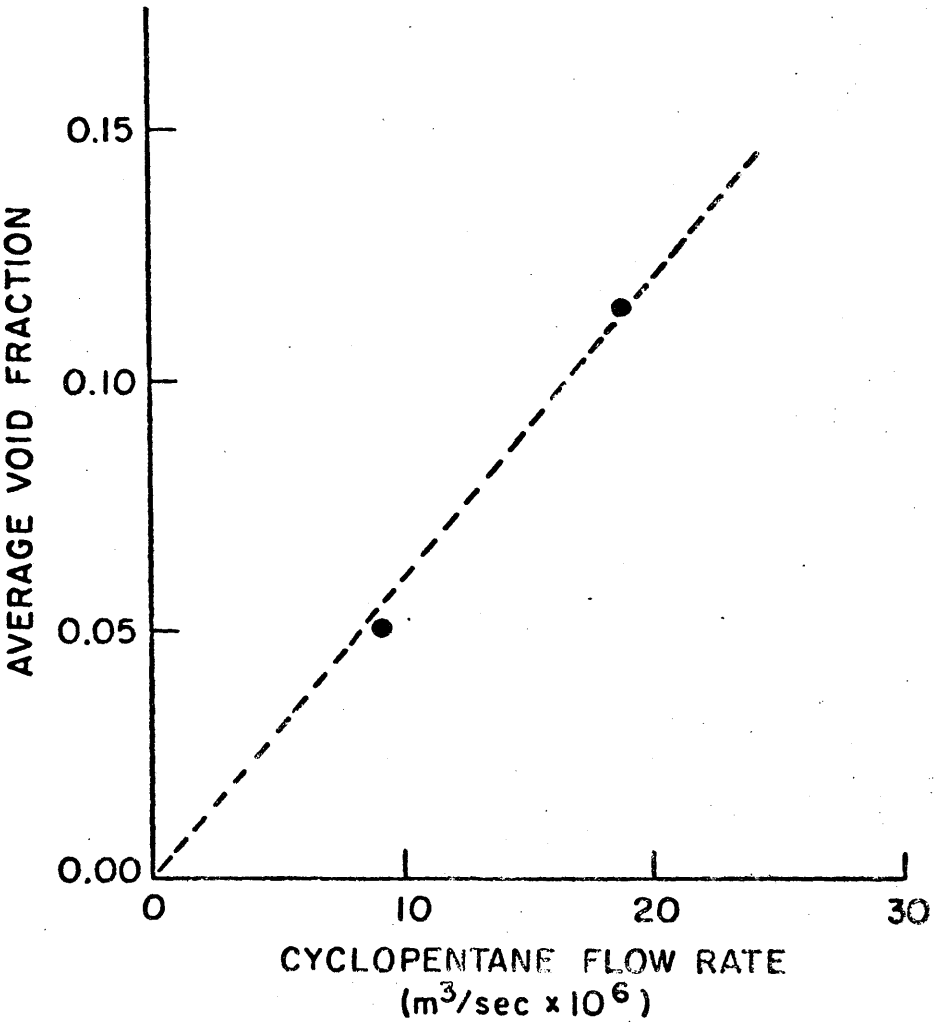

Figure 13. The Void Fraction vs. Evaporation Rate

for this system. Therefore, the formation of a layer of liquid cyclopentane above the water resulted from not only incomplete evaporation, but also from the accumulation of droplets that failed to nucleate. Furthermore, stratification of the layer is not immediate but results from the coalescence of tiny liquid droplets that accumulate gradually; consequently, there is a delay between the appearance and identification of incompletely vaporized cyclopentane. Finally, because the water temperature is decreasing steadily as evaporation proceeds, any lag in the thermocouple response or associated electronics will contribute to the error. However, because the data logger scanned the temperature twice a second, the four second time constant of the thermocouple was the limiting factor in determining the system response. In order to estimate and reduce the error, the minimum temperature difference was measured at least twice for each value of the water depth.

4.0 COMPARISON OF THEORY AND EXPERIMENT

4.1 Single Bubble Heat Transfer Coefficient

According to Section 2.4.1, the minimum temperature difference and water depth required for complete evaporation of the cyclopentane are related by the following set of equations in the absence of agglomeration

$$\left(\frac{\rho_{dl}}{\rho_{dv}}\right)^{m/3} - 1 = mBz \tag{64}$$

where

$$m = (1 - x)(y + 1) + 1 \tag{65}$$

$$B = 2 \frac{h_{bo}\Delta T}{U_o D_o L_d} \frac{\rho_{dl}-\rho_{dv}}{\rho_{dl}\,\rho_{dv}} \tag{66}$$

$$h_{bo} = {}^{k_c}/_{D_o}\, Nu_o \tag{67}$$

$$Nu_o = \gamma\, Re_o^x\, Pr_c^w \tag{68}$$

D_o and U_o are related according to

$$7\,(\tfrac{\pi}{4} D_o^2)\, U_o = \dot{W} \tag{69}$$

where $\dot{W}$ is the volumetric flow rate of the cyclopentane, and the factor of seven on the left hand side accounts for the seven holes in the distribution plate. For a volumetric flow rate of 6.31 cm^3/sec visual observation revealed that D_o was approximately 1.0 mm. Hence, according to Eq(69) U_o is approximately 100 cm/sec. Because

the droplets were injected with large initial velocities, and because they were too small to change from ellipsoidal to cap-shaped, the velocity remained relatively constant during the entire course of evaporation. Hence, the appropriate value of y is zero in Eqs(31) and (65).

Substituting Eqs(66)-(69) into Eq(64) yields

$$\left(\frac{\rho_{dl}}{\rho_{dv}}\right)^{m/3} - 1 = \frac{7\pi}{2} \frac{k_c \gamma Re_o^x Pr_c^w \Delta T}{\dot{W} L_d \rho_{dv}} z \tag{70}$$

where ρ_{dv} has been neglected compared to ρ_{dl}.

The Reynolds number is given by

$$Re_o = \frac{4\rho_c \dot{W}}{7\pi\mu_c D_o} \tag{71}$$

Substituting the appropriate values into Eq(71) yields $Re_o = 2340$, which suggests that heat transfer is dominated by turbulent convection in the wake of the droplets according to Section 2.3. Hence, the appropriate values of x and w in Eq(68) are approximately 0.8 and 1/3, respectively.

Substituting the appropriate values into Eq(70) yields

$$\gamma \Delta T z = 5.31 \tag{72}$$

where ΔT is in degrees Kelvin and z is in centimeters. For $\gamma = .0531$ Eq(72) appears to correlate the data in Figure 11 reasonably well. Furthermore, comparisons with Eqs(18) and (19)

suggest that .0531 is in reasonable agreement with the values of γ determined elsewhere.

The discrepancy at low values of the water depth probably results from the relatively increased contribution of surface evaporation above the water, which remains essentially constant while the volume decreases with the water depth. The discrepancy at small values of temperature difference is almost certainly due to the superheat requirement for nucleation.

4.2 The Effect of Agglomeration

In the second series of experiments conducted in this work, the pitch between the 0.5 mm diameter holes in the distribution plate was reduced from 5.0 to 2.9 cm, and the number of holes was increased from seven to nineteen.

These modifications resulted in increased void fractions. The average void fraction in the reaction vessel was determined according to the following formula

$$\bar{\alpha} = \frac{z - z_o}{z} \tag{73}$$

where z and z_o are the water depths measured during and prior to cyclopentane injection, respectively. The results are presented in Figure 13, and the apparent linear relationship between $\bar{\alpha}$ and $\dot{W}$ is characteristic of earlier experiments on direct-contact evaporation [19]. Since the void fraction generally has a linear

dependence on the superficial vapor velocity in two-phase flow experiments below the flooding condition, the results in Figure 13 are not unexpected. However, it is probable that $\bar{\alpha}$ would increase at a rate less than linear with $\dot{W}$ at higher values of $\dot{W}$, since a frothy flow with large bubbles, indicating flooding and agglomeration was observed in the upper portion of the vessel for cyclopentane flow rates in excess of 5 cm^3/sec. For a constant droplet velocity, the local void fraction in the absence of agglomoration is given by

$$\alpha = \frac{\dot{W} r^3}{A U_o} \tag{74}$$

where A is the flow area. Hence, the average void fraction is given by

$$\bar{\alpha} = \frac{\dot{W}}{A U_o} \frac{1}{z} \int_1^r r^3 \left(\frac{dz}{dr}\right) dr \tag{75}$$

But according to Eq(36)

$$z = K r^m \tag{76}$$

where K is a function of ΔT. Hence, Eq(75) becomes approximately

$$\bar{\alpha} = \frac{\dot{W}}{A U_o} \frac{m r^3}{m + 3} \tag{77}$$

which becomes

$$\bar{\alpha} = \frac{61.7}{A U_o} \dot{W} \tag{78}$$

for complete evaporation (r = 6) with m = 1.2 (x = 0.8 and y = 0). Assuming the droplets flow within the area circumscribed by the hexagonal array boundary on the distribution plate, A = 138 cm^2 in Eq. (78). Therefore,

$$\bar{\alpha} = 0.491 \frac{\dot{W}}{U_o} \tag{79}$$

where U_o is given in centimeters per second, and $\dot{W}$ is given in cubic centimeters per second. Comparing Eq(79) to Figure 12 implies that U_o = 90 cm/sec, which is approximately the same as the velocity in the first series of experiments. Similarly, D_o was approximately 1.0 mm in the second series of experiments.

According to Section 2.4.2, agglomeration increases the volume required for a given amount of evaporation for a fixed temperature difference over the values predicted on the basis of single bubble behavior above. This prediction was verified in this work since the single bubble result, Eqs. (64) - (68), with γ = 0.531, falls well below the data in Figure 12. Eqs. (36) and (57) yield

$$r_a^{m_o} - 1 = m_o B z_a \tag{80}$$

$$r^{m_a} - r_a^{m_a} = \frac{3 m_a}{y_a} (1 - \alpha_{max})^{1-x} B(z - z_a) \tag{81}$$

Combining Eqs(80) and (81) yields

$$\Delta T = \frac{K_1 + K_2}{z} \tag{82}$$

where

$$K_1 = \frac{\rho_{dv} U_o D_o^2 L_d}{k_c \, Nu_o} \; \frac{r_a^{m_o} - 1}{2m_o} \tag{83}$$

$$K_2 = \frac{\rho_{dv} U_o D_o^2 L_d}{k_c \, Nu_o} \; \frac{r^{m_a} - r_a^{m_a}}{\frac{6m_a}{y_a}(1-\alpha_{max})^{1-x}} \tag{84}$$

For complete evaporation

$$r^{m_a} = \left[(\rho_{dl}/\rho_{dv}) r_a^{y_a - 3}\right]^{\frac{m_a}{y_a}} \tag{85}$$

During the post-agglomeration stage of evaporation, the bubbles become large enough to assume the characteristic cap shape; consequently, y_a is one half since the velocity of cap shaped bubbles is proportional to the square root of their diameter. m increases with y according to Eq(38), so m_a becomes 1.3, although x remains constant at 0.8. Substituting the appropriate values in Eqs(83) and (84) yields

$$K_1 = 6.94 \; (r_a^{1.2} - 1) \tag{86}$$

$$K_2 = 1.07 \; (1-\alpha_{max})^{-0.2} \left[(216 r_a^{-2.5})^{2.6} - r_a^{1.3}\right] \tag{87}$$

Selecting $r_a = 5.1$, which implies that $\alpha_{max} = 0.108$ according to Eq. (74), yields reasonably good agreement with the minimum water temperature data for cyclopentane flow rate $\dot{W} = 9.47$ cm^3/sec in Figure 12. Furthermore, since

$$\bar{\alpha} = \frac{z_a}{z}\left(\frac{1}{z_a}\int_0^{z_a}\alpha dz\right) + \frac{z-z_a}{z}\,\alpha_{max} \qquad (88)$$

substituting Eqs(77), (80) and (81) into Eq(88) and simplifying yields $\bar{\alpha} = 0.058$ for $\dot{W} = 9.47$ cm^3/sec, which agrees reasonably well with the data point in Figure 13 at $\dot{W} = 9.47$ cm^3/sec.

Although $\alpha_{max} = 0.108$ is smaller than data obtained in isothermal and pool boiling experiments, in this work there was visual evidence that agglomeration was encouraged by the method of injection. Considerable drafting in the wake was observed as the cyclopentane jets broke up into discrete droplets. Nucleation appeared to induce the break-up of the jets, and droplets within a few diameters of one another frequently coalesced as the drafter would overtake the leader. Therefore, it is plausible that the large local droplet density and drafting in the vicinity of the cyclopentane jets are responsible for promoting agglomeration, although the averaged void fraction may be quite small.

4.3 Summary of Recommended Heat Transfer Coefficients

The experimental results indicate that the mathematical model is capable of predicting volumetric heat transfer coefficients using typical single droplet heat transfer correlations in conjunction with a realistic constraint on the void fraction to account for agglomeration. Until a more universally successful formula is developed, the use of Eq. (20) is recommended with $\gamma = .05$ to 0.1, $x = 0.8$ and $w = 1/3$ to reflect the turbulent nature of the process. The use of Eq. (31) is recommended for calculating the droplet velocity. The value of y should be selected to reflect the actual velocity dependence on the diameter ratio, but y must be greater than zero during the post-agglomeration stage to provide the mechanism responsible for agglomeration in the model. Finally, it is recommended that α_{max} be prescribed on the basis of direct experimental evidence whenever possible or on the basis of typical maximum values reported in the literature for the expected flow regime.

5.0 APPLICATION OF THE MODEL TO UNPROTECTED LOF ACCIDENTS IN LMFBR

5.1 Introduction

The systematic and rigorous analysis of unprotected Loss Of Flow (LOF) accidents in Liquid Metal Fast Breeder Reactors (LMFBR) is extremely complicated due to both phenomenological uncertainties and the strong interdependence of phenomena. Therefore, large, expensive computer codes are required to properly analyze the problem deterministically. However, because of the aforementioned uncertainties, recent investigations have been concentrated on determining the relative sensitivity of the calculated consequences to variations in the effects of certain phenomena. Those sensitivity studies efficiently enable the researchers to identify the important phenomena and are helpful in directing the efforts of subsequent work.

Fuel-to-steel heat transfer is one phenomenon that warrants further investigation according to recent work at the Los Alamos Scientific Laboratory [21] and the Brookhaven National Laboratory [27].

This work was initiated to investigate the relative importance of fuel-to-steel convective heat transfer in mitigating the consequences of an LOF accident in LMFBRs. In this section the model developed in Section 2.0 will be applied to calculate the expected values of the volumetric heat transfer coefficient for such situations. These values will be compared to the values obtained assuming pure conduction, since the current version of the SIMMER code is based on a conduction model for heat transfer and the possible implications and significance of the differences will be discussed.

5.2 LOF Basic Sequences

Prior to a discussion of the role of fuel-to-steel heat transfer a brief description of the predicted LOF accident scenario may lend perspective to this work. A hypothesized transition phase accident sequence flow chart is presented in Figure 14. It traces the various stages of the accident, highlights the expected major events, and indicates crucial junctions along the accident progression [27].

During the initiation phase it is assumed that the coolant pumps lose power and "coast down" so that the flow of sodium through the core decays. Since it is also assumed that the protective systems fail to scram the reactor, the sodium heats up until it begins to boil. Boiling is predicted to occur about 10 or 15 seconds following pump failure, and complete voiding follows in a matter of seconds. Clad melting occurs between 0.5 and 2 - 3 seconds after voiding, depending upon the void coefficient of reactivity.

The fuel disruption phase follows clad melting by between 0.15 and 3 - 4 seconds, again, depending upon the void coefficient. The timing is important because it determines whether or not there is sufficient time for steel blockages to form from clad relocation above and below the core. Blockages would restrict axial fuel expansion and limit the associated reactivity loss. The motion of the fuel following its disruption is extremely important in determining the subsequent energetics. Fuel slumping and recompaction will result in a move reactive configuration and the possibility of an energetic disassembly. Fuel dispersal will decrease the reactivity and probably

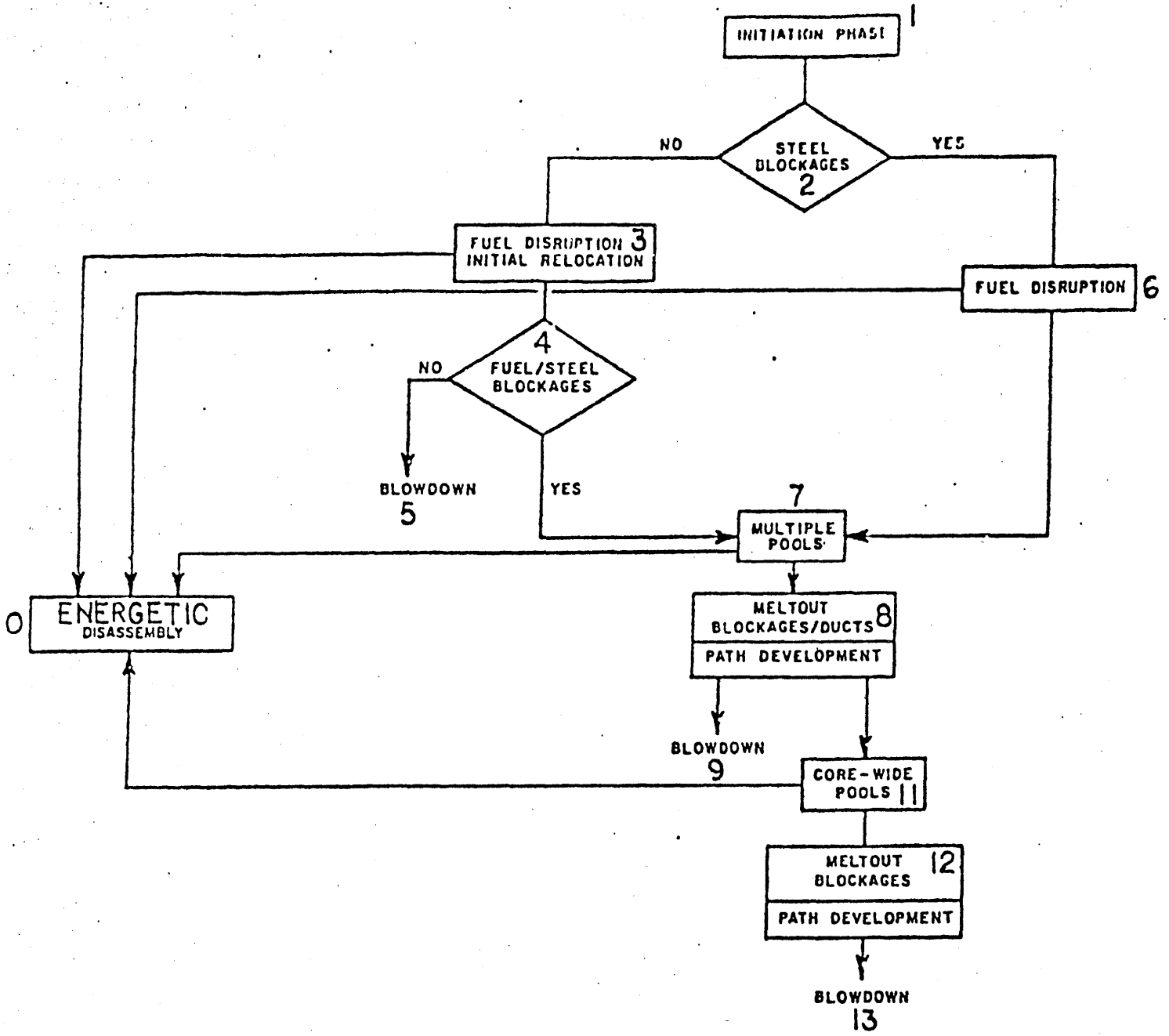

Figure 14. Transition Phase Accident Sequence Paths [27]

lead to a more benign conclusion. The dispersal of fuel depends upon both the existence of a dispersive pressure source and relocation paths from the core. Possible pressure sources include fission gas expansion and steel and/or fuel vaporization, while the existence of paths depends upon fuel and steel penetration and freezing above the core.

If the accident ends in neither a benign blowdown nor an energetic disassembly following fuel disruption, the accident will enter the so-called "transition phase." In the transition phase the core gradually melts-down, forming multiple subassembly scale pools which may combine to form a core-wide pool following duct wall melt-in. The behavior of these pools depends upon heat transfer to the boundaries, transient sensible heating due to pressurization and heat transfer to subcooled steel from duct wall melt-in. If the heat losses exceed the heat generation, vaporization will cease and the boiled-up pools will collapse into a more reactive configuration. However, as long as vaporization can sustain a boiled-up configuration a nonenergetic blowdown is possible following meltout of the fuel/steel blockages above the core. Steel vaporization is expected to provide the dispersive pressure source during the transition phase.

5.3 Significance of Fuel-to-Steel Heat Transfer

In the absence of fuel-to-steel heat transfer following the core meltdown, it is expected that the fuel would quickly begin to vaporize through decay heating. Flow area changes and friction in the above core structure will limit the work energy to 22.7 MJ for a 5100 °K core

expansion in the Clinch River Breeder Reactor [21]. Sensible heating of the molten steel in the core, however, could be an important heat sink limiting the temperature rise. The effectiveness of this process in reducing fuel vaporization will depend upon the rate of heat transfer, and parametric calculations indicate that convection effects due to low relative velocities can result in an order of magnitude increase in the fuel-to-steel heat transfer rate when compared to pure conduction [21]. The resuling decrease in the rate of expansion can significantly reduce the work potential. However, there is also evidence suggesting that rapid fuel-to-steel heat transfer in the core can result in steel vaporization. In fact, the steel can become the working fluid rather than just a heat sink, with an increase in the work potential as a result [21]. Consequently, the rate of steel vaporization could be of considerable importance in determining the accident energetics, so that modeling fuel-to-steel boiling heat transfer to ensure conservatism becoms a concern.

5.4 Implications of the Present Work

The results of this work indicate that the accident analysis codes in their present form may not be ensuring sufficient conservatism in situations where steel vaporization in a molten pool is significant. Specifically, the codes may be underestimating the rate of steel vaporization due to inherent modeling limitations. At present the SIMMER-II code [2] does not admit relative velocities between liquid components nor does it allow a steel droplet to

contain both liquid and vapor. Consequently, vaporization occurs as a result of conduction to liquid steel droplets, and the vapor generated is assumed to enter the vapor field immediately. Therefore, the liquid steel droplets shrink as evaporation proceeds, so that the contact area for liquid fuel-to-liquid steel heat transfer must also shrink. However, according to a simple criterion presented by Mori [22], the vapor will remain attached to the liquid steel droplets if

$$\sigma_f - (\sigma_s + \sigma_{fs}) < 0$$

and

$$\sigma_s - (\sigma_f + \sigma_{fs}) < 0$$

where σ_f is the surface tension of fuel, σ_s is the surface tension of steel and σ_{fs} is the interfacial surface tension between liquid fuel and liquid steel. The spreading coefficients characterizing a UO_2-steel system indicate that the liquid steel will form a thin film that partially surrounds the vapor core of the expanding two-phase steel droplets (see Figure 3). This configuration results in a substantially larger liquid fuel-to-liquid steel heat transfer area than the configuration assumed by SIMMER-II. Furthermore, because the mean density of an expanding two-phase steel droplet must be decreasing, the buoyancy driven relative velocity of the droplet should increase. Therefore, both the heat transfer area and the magnitude of the resulting convective heat transfer may be underpredicted in the current versions of the co-es unless the multiplicative correction factors

employed are selected sufficiently large. Since liquid fuel-to-liquid steel heat transfer in a pool of molten UO_2 and the possibility of boil-up in the pool due to steel vaporization are of such potential importance to the subsequent course of the accident sequence, there is considerable incentive to model these phenomena as accurately as possible, or at least to guarantee conservatism in simplified approximations.

Table 2 lists the thermophysical properties of molten fuel and steel, and Table 3 lists estimated parameter ranges for LMFBR core disruptive accident analyses. It must be noted, however, that vapor densities and saturation temperatures are pressure dependent.

Substituting the appropriate values in Eq(12) yields

$$U = 7.68\ (D_o\ \nabla p\ r)^{1/2}\ \text{m/sec} \tag{89}$$

where D_o is given in meters and ∇p in MPa/m. The Reynolds number is given by

$$Re = 1.74 \cdot 10^6\ U_o D_o r^{3/2} \tag{90}$$

and always exceeds 1500. The Prandtl number of molten UO_2 is approximately one, so Eq(20) becomes

TABLE 2

THERMOPHYSICAL PROPERTIES OF MOLTEN UO_2 AND STAINLESS STEEL

Property	Units	UO_2	Stainless Steel
Melting Temperature	°K	3120	1680
Boiling Temperature	°K	3690	3090
Heat of Vaporization	KJ/kg	1930	6280
Thermal Conductivity	W/m K	2.9	31
Liquid Density	kg/m^3	8700	7000
Vapor Density	kg/m^3		1.0
Specific Heat	J/kg K	500	800
Viscosity	kg/ms	.005	.006

TABLE 3

ESTIMATED PARAMETER RANGES FOR LMFBR

CORE DISRUPTIVE ACCIDENT ANALYSES

Parameter	Units	Range	Remarks
Initial Steel Droplet Diameter D_o	cm	0.5 - 2.0	lower value = can wall thickness higher value = Taylor instability value
Initial Steel Volume Fraction α_o	—	0 - 20%	depends on amount of steel in the core and the scenario
Pressure Gradient ∇p	MPa/m	0.1 - 10	depends on energetics (vapor pressures) and rate of expansion
Fuel-Steel Temperature Difference ΔT	°K	50 - 600	depends on energetics with T_{steel} at saturation $\Delta T_{max} = T_{UO_2}$ - $T_{steel_{sat.}}$ $\Delta T_{min} = T_{UO_{2_{melt}}}$ - $T_{steel_{sat.}}$

$$Nu = \gamma \, Re^{x} \tag{91}$$

$$h_{bo} = 2.9 \, (1.74 \cdot 10^{6})^{x} \, \gamma \, U_o^{x} D_o^{x-1} \quad \frac{W}{m^2 K} \tag{92}$$

Substituting the appropriate values for $\rho_{d\ell}$, ρ_{dv}, L_d and h_{bo} into Eq. (35) yields

$$B = 9.22 \cdot 10^{-7} \, (1.74 \cdot 10^{6})^{x} \, \gamma U_o^{x-1} D_o^{x-2} \Delta T \quad m^{-1} \tag{93}$$

Assuming laminar flow implies x = 0.5 while $\gamma \simeq 0.27$; hence, Eqs. (92) and (93) become

$$h_{bo} = 1.03 \cdot 10^{3} \, U_o^{0.5} D_o^{-0.5} \quad \frac{W}{m^2 K} \tag{94}$$

$$B = 3.28 \cdot 10^{-4} \, U_o^{-0.5} D_o^{-1.5} \Delta T \quad m^{-1} \tag{95}$$

Assuming turbulent flow implies x = 0.8 while $\gamma \simeq 0.1$; hence, Eqs. (92) and (93) become

$$h_{bo} = 2.85 \cdot 10^{4} \, U_o^{0.8} D_o^{-0.2} \quad \frac{W}{m^2 K} \tag{96}$$

$$B = 9.06 \cdot 10^{-3} \, U_o^{-0.2} D_o^{-1.2} \Delta T \quad m^{-1} \tag{97}$$

For pure conduction, x = 0 while $\gamma = 2$; hence, Eqs. (92) and (93) become

$$h_{bo} = 5.8 \, D_o^{-1} \quad \frac{W}{m^2 K} \tag{98}$$

$$B = 1.84 \cdot 10^{-6} \, U_o^{-1} D_o^{-2} \Delta T \quad m^{-1} \tag{99}$$

Eqs. (41) and (62) are used to evaluate the volumetric heat transfer coefficient as a function of α_o for core disruptive accident

conditions in Figure 15. α_{max} has been set to 0.50 in Eq(62), and z has been set to 1.0 meter, which is typical of LMFBR core dimensions. For such conditions Eq(62) becomes approximately

$$h_v(z) \simeq \frac{2h_{bo}}{D_o Bz}\left[\frac{3}{y}(1-\alpha_{max})^{1-x}\, mBz\right]^{y/m} \frac{\alpha_{max}}{1-\alpha_{max}} \qquad (100)$$

As a function of U_o, D_o and ΔT, Eq(100) can be written

$$h_v = K\, U_o^{1+(y/m)(x-1)} D_o^{(y/m)(x-2)} \Delta T^{(y/m)-1} \qquad (101)$$

The values of the exponents in Eq(101) are listed in Table 4 for conduction (x=0), laminar convection (x=0.5) and turbulent convection (x=0.8) for y=0.5 (velocity proportional to $r^{1/2}$). In all three cases h_v increases with U_o, but the dependence is strongest for turbulent convection. Similarly, for all three cases h_v increases as D_o decreases, and, again, the dependence is strongest for turbulent convection. h_v increases with U_o because the amount of steel passing through the volume in a fixed time increases with U_o, and it decreases with D_o because large droplets have smaller values of h_b than small droplets. h_v decreases as ΔT increases because agglomeration occurs sooner, and agglomeration tends to suppress heat transfer. Consequently, Eq(41), the pre-agglomeration result, increases with ΔT because the convective effects and surface area increase with droplet expansion, and droplet expansion increases with ΔT.

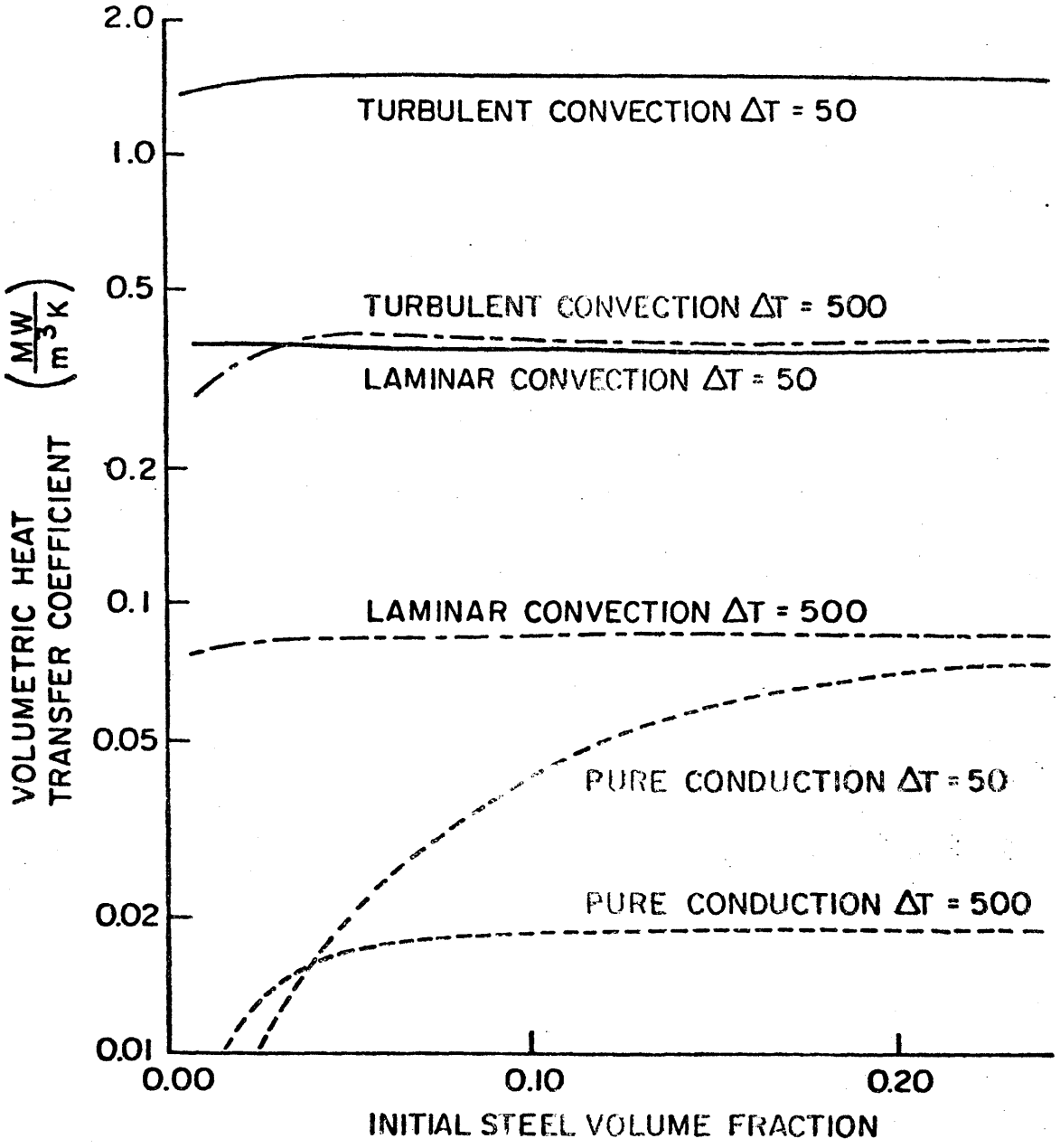

Figure 15. The Volumetric Heat Transfer Coefficient for a Steel-UO_2 System

TABLE 4

EXPONENTS FOR EQ. (101)

Heat Transfer Mode	$1+y/m(x-1)$	$y/m(x-2)$	$y/m-1$
Conduction $x=0,\ m=2.5$	0.8	-0.4	-0.8
Laminar convection $x=0.5,\ m=1.75$	.857	-.429	-.715
Turbulent convection $x=0.8,\ m=1.3$	.924	-.462	-.615

Referring to Figure 15 indicates that $h_v \Delta T$ is on the order of 100 MW/m^3. Since a typical LMFBR (Clinch River Breeder Reactor Besign Bases) will have a power density of about 300 MW/m^3 in the core at full power, fuel-to-steel boiling heat transfer can lead to transferring a substantial fraction of the total steady-state power to the steel in a short time.

5.5 Time to Vaporize Steel

As previously stated, the importance of steel vaporization in dispersing molten fuel depends upon how quickly the steel reaches its saturation temperature. To obtain an order of magnitude estimate of the time required for the steel to reach its saturation temperature, consider the following simplified analysis.

In order to simplify the calculations, the spherical droplets of subcooled steel in the molten UO_2 will be approximated by plane geometry; however, the dimensions will be selected to preserve the ratio of volume to surface area of the droplets. Furthermore, because the thermal conductivity of liquid steel is an order of magnitude larger than that of molten UO_2, the temperature within the steel is assumed to ba spatially uniform. Therefore, the following equations are sufficient to describe the situation depicted in Figure 16 assuming conduction limited heat transfer

$$\frac{\partial T}{\partial t} = \alpha_f \frac{\partial^2 T}{\partial x^2} + S' \qquad x > 0 \qquad (102)$$

$$\lim_{x \to \infty} \frac{\partial T}{\partial x} = 0 \qquad x = 0 \qquad (103)$$

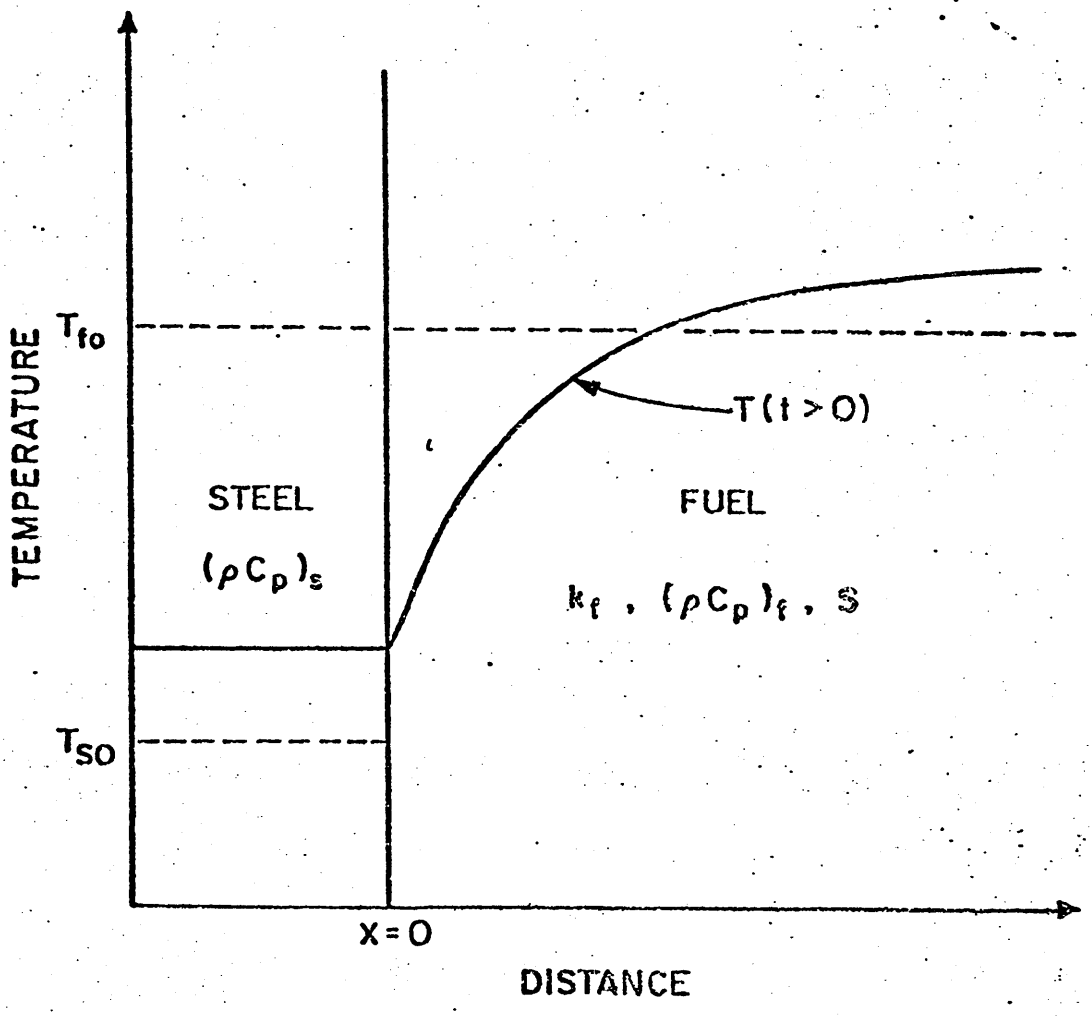

Figure 16. A Simplified Model for Calculating the Liquid Steel Temperature Upon Contact with Internally Heated Fuel

$$\frac{\partial T}{\partial x} = \frac{(\rho C_p)_s}{k_f} \left(\frac{V}{A}\right)_s \frac{\partial T}{\partial t} \qquad x = 0 \tag{104}$$

$$T = T_{fo} \qquad x > 0, \quad t = 0 \tag{105}$$

$$T = T_{so} \qquad x = 0, \quad t = 0 \tag{106}$$

where $\alpha_f = k_f/(\rho C_p)_f$, $S' = S/(\rho C_p)_f$ and S is the volumetric power density in the fuel, while the subscripts f and s denote fuel and steel, respectively. Eq(102) describes the evolution of the temperature profile in the fuel, while Eq(103) implies that the temperature in the fuel is spatially uniform far from the steel heat sink. Eq(104) is the boundary condition at the fuel-steel interface, and it states that the temperature of the steel, T at x=0, increases as a result of the heat flux from the fuel, which is directly proportional to $\partial T/\partial x$ evaluated at x=0. Eqs (102)-(106) were solved using Laplace Transforms to yield

$$T_s = T_{so} e^{K^2 t} \operatorname{erfc}(K\sqrt{t}) + T_{fo}(1 - e^{K^2 t} \operatorname{erfc}(K\sqrt{t}))$$

$$+ S'(t - K^{-2}(2K\sqrt{t/\pi} + e^{K^2 t} \operatorname{erfc}(K\sqrt{t}) - 1)) \tag{107}$$

where $K = \sqrt{\alpha_f}(A/V)_s(\rho C_p)_f/(\rho C_p)_s$ and erfc(x) is the complementary error function defined as

$$\operatorname{erfc}(x) = \frac{2}{\sqrt{\pi}} \int_x^\infty e^{-y^2} dy$$

Assuming the fuel is at its melting point initially, $T_{fo} = 3150^oK$. The melting point of steel is about 1700^oK, and its boiling point is about 3100^oK. Eq(107) was used to calculate the time required

to reach the saturation temperature of steel for various values of the power and initial steel temperature assuming that the fuel was at its melting temperature initially and the steel droplets were 1.0 cm in diameter initially. The results are plotted in Figure 17. Obviously, the amount of time required to boil the steel is very sensitive to the power level. For levels less than tem times full power ($\sim$300 MW/m), the time required exceeds one second for subcooling greater than 250 °K, and at full power ($\sim$300 MW/m) the time required exceeds one second for subcooling greater than 50 °K.

Including the effect of convection in the preceding analysis would almost certainly reduce the time required to boil the steel; consequently, it appears that steel vaporization could be of importance if the power level is high enough (greater than ten times full power) or if the steel is only slightly subcooled (less than about 50^{o}K) when the molten pool forms.

With $h_v \Delta T = 100$ MW/m^3, it requires only about one half second to vaporize one percent of the steel in the core. Hence, steel vaporization, if it occurs, would certainly be an important pressure source, and it may contribute significantly to the work potential generated during a LOF accident in an LMFBR.

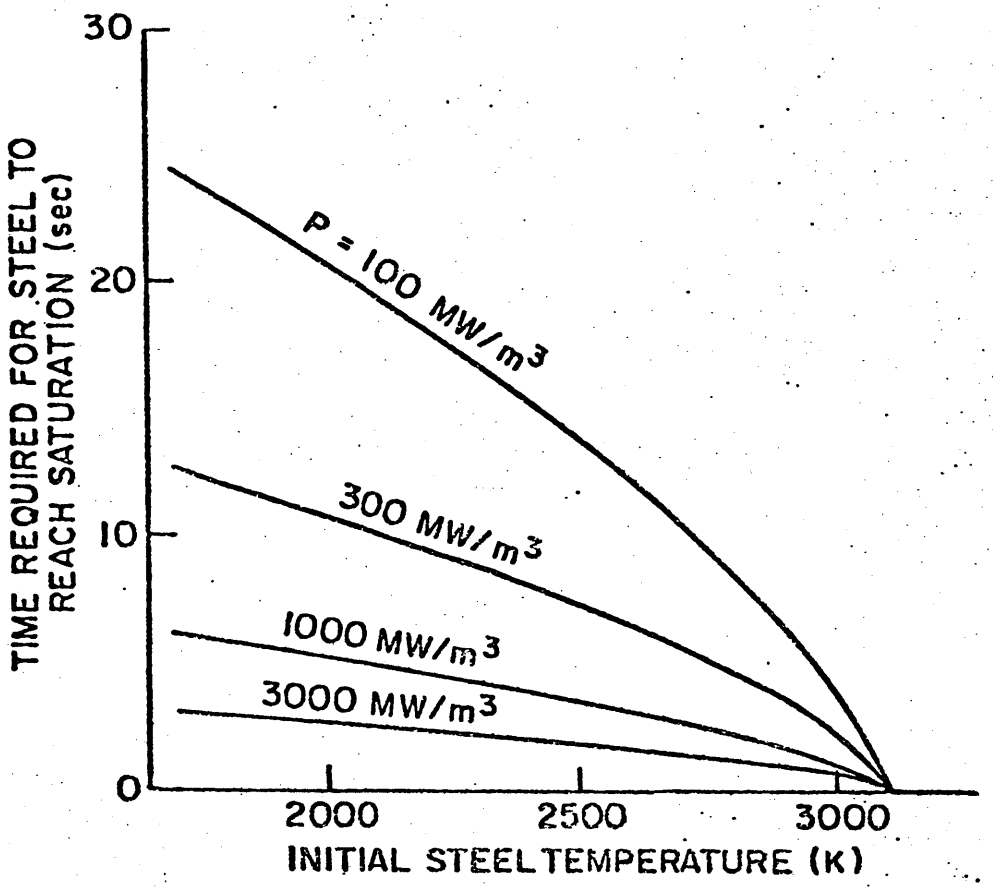

Figure 17. An Estimate of the Time Required to Heat 1.0 cm Diameter Steel Droplets to the Saturation Temperature

6.0 CONCLUSION AND RECOMMENDATIONS FOR FUTURE WORK

The mathematical model for the volumetric heat transfer coefficient in direct contact boiling developed in this work is reasonably successful in predicting the experimental results obtained. The value of α_{max} which was selected to correlate the data for the minimum temperature difference required for complete evaporation versus water depth resulted in an average α prediction which agreed quite well with the experimentally determined value. Hence, there is optimism that the physical basis of the mathematical model is correct.

However, since data acquisition over a large range of evaporation rates was impossible in this work, more experiments should be conducted to test the model over a broader range of flow rates. Furthermore, since the predictive capability of the model is not limited to complete evaporation, experiments which varying degrees of evaporation should be conducted to test the model. Experiments with artificially induced nucleation should also be conducted to eliminate the uncertainty associated with nucleation and superheating.

It would also be convenient if a means for creating a more uniform initial droplet distribution could be devised to eliminate the premature agglomeration associated with jet injection. Perhaps increasing the density of holes in the distribution plate would alleviate the problems associated with jets.

Data from this work suggests that the value of α_{max} that correlates the experimental ΔT_{min} vs. water depth increases with $\dot{W}$, the cyclopentane

flow rate. Furthermore, there is evidence that the same value of α_{max} can be used to correlate the data for $\bar{\alpha}$ vs. $\dot{W}$, although it was impossible to obtain data over a broad enough range of $\dot{W}$ in this work to verify this conclusively.

The results of this work indicate that it is important to model steel vaporization accurately in core disruptive accidents, because the rate could be sufficient to generate very high vapor pressures that determine the ultimate consequences of the accidents. Furthermore, the simple analysis performed in this work to calculate the time required to raise the steel temperature to saturation indicates that liquid-liquid fuel-to-steel heat transfer should also be modeled carefully, including convection, in view of the consequences of steel vaporization. The major concern identified in this work is that separated phase modeling may result in underpredicting the liquid-liquid interfacial area and, consequently, the heat transfer rate between fuel and steel in a molten pool.

APPENDIX A

In the text, Eq(2) was solved for cases in which the first term is negligible. Here Eq(2) will be solved for cases in which the second term is negligible compared to the first. It is assumed that ∇p is large and that U_0 is insignificant. Under such conditions, although the first term in Eq(2) will be large due to the rapid acceleration, the second term will be comparatively small until U^2 becomes significant. Consequently, the solution derived here will describe the early behavior or the bubble velocity, while Eq(4) is appropriate during the later stages of growth. After obtaining a solution under either assumption, it is prudent to compare the magnitude of terms in Eq(2) to verify the assumption.

Negelcting the second term in Eq(2) yields

$$(\tfrac{1}{2}\rho_c + \rho_d)\frac{dU}{dt} = \nabla p(1-\rho_d/\rho_c) \qquad \text{(A-1)}$$

Since $\rho_d = \rho_{d_1} r^{-3}$ and r increases very rapidly with the vapor mass fraction X_v (see Figure B-1 in Appendix B), it is permissible to neglect ρ_d compared to ρ_c in Eq(A-1)

$$\frac{dU}{dt} = \frac{2\nabla p}{\rho_c} \qquad \text{(A-2)}$$

Although the solution of Eq(A-2) in terms of t is trivial for constant ∇p

$$U = \frac{2\nabla p}{\rho_c} t + U_0 \tag{A-3}$$

it is more useful to express U as a function or r.

$$\frac{dU}{dr}\left(\frac{dr}{dt}\right) = \frac{2\nabla p}{\rho_c} \tag{A-4}$$

Substituting $U(^{dr}/_{dz})$ from Eq(29) for $^{dr}/_{dt}$ in Eq(A-4) above yields

$$\frac{dU}{dr} = \frac{2\nabla p}{\rho_c}\left[\frac{D_0 L_d}{2h_b \Delta T}\ \frac{\rho_{d1}\rho_{dv}}{\rho_{d1}-\rho_{dv}}\right] \tag{A-5}$$

Substituting Eq(32) for h_b yields

$$U^x dU = \frac{\nabla p D_0^{2-x} L_d}{\rho_c H \Delta T}\ \frac{\rho_{d1}\rho_{dv}}{\rho_{d1}-\rho_{dv}}\ r^{1-x}\, dr \tag{A-6}$$

or

$$\left(\frac{U}{U_0}\right)^x d\left(\frac{U}{U_0}\right) = \frac{\nabla p}{\frac{1}{2}\rho_c U_0^2}\ \frac{r^{1-x} dr}{B} \tag{A-7}$$

where B is defined by Eq(35). Integrating Eq(A-7) yields

$$U = U_0\left[\frac{\nabla p}{\frac{1}{2}\rho_c U_0^2}\ \frac{(x+1)(r^{2-x}-1)}{(2-x)B} + 1\right]^{\frac{1}{x+1}} \tag{A-8}$$

By assumption U_0 is insignificant so that heat transfer is by conduction primarily. Hence, substituting $x = 0$ and simplifying Eq. (A-8) yields

$$U = \frac{\rho_{dv} L_d D_0^2 \nabla p}{4 \rho_c k_c \Delta T} (r^2-1) \qquad \text{(A-9)}$$

The assumption that the second term in Eq(2) is negligible is equivalent to

$$\frac{A_p}{V} C_D \frac{\rho_c U^2}{2} << \nabla p \qquad \text{(A-10)}$$

Substituting Eq(A-9) into Eq(A-10) and simplifying yields

$$\frac{3 C_D \rho_{dv}^2 L_d^2 D_0^3 \nabla p}{16 \rho_c k_c^2 (\Delta T)^2} \quad \frac{(r^2-1)^2}{r} << 1 \qquad \text{(A-11)}$$

Eq(A-9) is only valid when Eq(A-11) is satisfied.

As an example, consider a stainless steel - UO_2 system. Substituting the appropriate thermophysical properties form Table into Eq(A-11) yields

$$\frac{C_D \nabla P}{(\Delta T)^2} \frac{(r^2-1)^2}{r} << 10^{-8} \qquad \text{(A-12)}$$

where ∇p is in MPa/m and ΔT is in K the value of C_D depends upon the Reynolds number

$$Re = 1.74 \times 10^6 \, Ur \tag{A-13}$$

where U is in m/s. According to Eq(A-9)

$$U = 6.22 \times 10^3 \frac{\nabla p}{\Delta T} (r^2-1) \quad m/s \tag{A-14}$$

where ∇p is in MPa/m and ΔT is in K. As typical values, consider ∇p = 1 MPa/m and ΔT = 600°K. Then according to Eq(A-14)

$$U = .10(r^2-1) \quad m/sec \tag{A-15}$$

while

$$Re = 1.74 \times 10^7 \, r(r^2-1) \tag{A-16}$$

and

$$4 \, C_D \frac{(r^2-1)^2}{r} << 10^{-2} \tag{A-17}$$

For $r > 1 + 3 \times 10^{-6}$, $Re > 10^2$ and $C_D < 1$, so the condition

$$\frac{(r^2-1)^2}{r} << 2.5 \times 10^{-3} \tag{A-18}$$

is conservative. Eq(A-18) is satisfied for $3 \times 10^{-6} < r-1 < 2.5 \times 10^{-3}$.

Obviously the amount of evaporation which occurs in this range is insignificant, and Eq(4) can be used over the entire range of r. Since the hydrostatic head in a pool of molten UO_2 results in a pressure gradient of almost 0.1 MPa/m, it seems unlikely that Eq(A-10) would ever be satisfied over any significant range of r. Consequently, throughout the analysis in section 5.0, Eq(4) is used to calculate the velocity of steel droplet/bubbles in UO_2.

APPENDIX B

B.0

As mentioned previously, during the direct-contact evaporation of droplets both the dispersed phase liquid film inside the droplet and the continuous phase boundary layer surrounding the droplet contribute to the overall thermal impedance. Depending upon the comparative thermophysical properties of the two components and their effective thermal boundary layer thicknesses, however, the resistance of one of the components may be relatively unimportant. Presently, research is being conducted to determine criteria for ignoring the resistance of one component relative to the other. Although the results are not quite conclusive, there is considerable evidence to suggest that for most liquids it is permissable to ignore the resistance of the dispersed phase liquid film after only a small fraction evaporates. Here arguments will be presented to support this contention and to offer some justification for the use of Eq(20).

Consider a butane-water system such as the one used by Nazir [10]. The relevant thermophysical properties of the two components are presented in Table B1. If x_v represents the vapor mass fraction inside the droplet, then it is easy to show that x_v is related to the equivalent spherical diameter ratio r by

$$1-x_v = \frac{\rho_{dl}-\rho_{dv}\, r^3}{\rho_{dl}-\rho_{dv}} \qquad \text{(B-1)}$$

Since $\rho_{dl}/\rho_{dv} = 216$ for butane, r increases very rapidly with x_v as shown in Figure B-1. Nazir reported that for r>2 the droplet assumed a spherical cap shape (see Figure 4 in the text) with a constant value of $\theta_{cap}=55°$. Since r=2 corresponds to only 3.3% evaporation, it can reasonably be assumed that the details of the heat transfer process are unimportant for r<2. Consequently, in this analysis the heat transfer coefficient for the liquid inside a spherical cap shaped bubble will be calculated for various assumptions concerning the disposition and motion of the liquid in the droplet. These values will then be compared to Nazir's experimental values of the overall heat transfer coefficient as a function of r to show that the internal thermal resistance is negligible over most of the range of r.

B.1 Conduction Models

Perhaps the most conservative assumption is that the dispersed phase liquid forms a stagnant film of uniform depth at the bottom of the droplet. Any departure from this condition would probably result in spreading or motion within the film and enhance heat transfer. Referring to Figure 4 in the text and performing a few simple

calculations yields

$$\left(\frac{R_{cap}}{R_{es}}\right)^3 = \frac{4}{(1-\cos\theta_{cap})(1-\cos\theta_{cap}+\sin^2\theta_{cap})} \quad \text{(B-2)}$$

$$V_{dl} = \frac{4\pi}{3} R_0^3 \left[\frac{\rho_{dl}-\rho_{dv}r^3}{\rho_{dl}-\rho_{dv}}\right] \quad \text{(B-3)}$$

$$A = \pi (R_{cap} \sin\theta_{cap})^2 \quad \text{(B-4)}$$

$$R_{es} = R_{es_0} r \quad \text{(B-5)}$$

where V_{dl} is the volume of the liquid in the droplet, A is the area of the bottom of the droplet and R_{es} and R_{es_0} are the instantaneous and initial values of the equivalent spherical radius, respectively. Combining Egs (B-3) and (B-4) yields

$$\delta = \frac{V_{dl}}{A} = \frac{\sqrt[3]{4}}{3} \frac{(1-\cos\theta_{cap})^{2/3}(1-\cos\theta_{cap}+\sin^2\theta_{cap})^{2/3}}{\sin^2\theta_{cap}} \cdot \left[\frac{\rho_{dl}-\rho_{dv}r^3}{\rho_{dl}-\rho_{dv}}\right] \frac{R_{es_0}}{r^2} \quad \text{(B-6)}$$

or since $\theta_{cap} = 55°$ and $D_{es_0} = 3.75$ mm

$$\delta = 0.891/r^2 \left[\frac{216-r^3}{215}\right] \text{ mm} \quad \text{(B-7)}$$

Then defining

$$h_{iu} = \frac{k_{di}}{\delta} \frac{A}{A_b} \tag{B-8}$$

where

$$A_b = \pi D_{es}^2$$

yields

$$h_{iu} = .0842\ r^2\ [\frac{215}{216-r^3}]\ \frac{kW}{m^2 {}^\circ K} \tag{B-9}$$

Referring to Figure B-2 it appears that even under the most conservative assumption the heat transfer coefficient inside the drop is of the same order of magnitude as the observed values of the overall heat transfer coefficient for $r > 3$, which corresponds to 12% evaporation.

As the next level of sophistication, consider the case of a stagnant film with a concave shaped surface

$$\delta = \delta_m + (\delta_M - \delta_m)(r/R_{cap})^n \tag{B-10}$$

It is not difficult to show that

$$\bar{\delta} = \delta_m + \frac{2}{n+2} (\delta_M - \delta_m) \tag{B-11}$$

where $\bar{\delta}$ is the area averaged value of δ and δ_m and δ_M are the minimum and maximum values of δ, respectively. Since $\bar{\delta}$ must be a constant for a given value of r, irrespective of the shape of the film, to conserve the liquid volume, Eqs (B-7) and (B-11) must be equal as functions of r. However, the heat transfer coefficient is defined as

$$h_i = k_{dl} \overline{(1/\delta)} \frac{A}{A_b} \tag{B-12}$$

and $\overline{(1/\delta)} \neq 1/\bar{\delta}$, in general; therefore, it is necessary to calculate $\overline{(1/\delta)}$

$$(\frac{\bar{1}}{\delta}) = \frac{1}{\pi R_{cap}^2} \int_0^{R_{cap}} 2\pi r \frac{1}{\delta} dv \tag{B-13}$$

and substitute the result into

$$h_i = h_{iu} \bar{\delta} (\frac{\bar{1}}{\delta}) \tag{B-14}$$

where h_{iu} is the heat transfer coefficient assuming a uniform value of δ, i.e. Eq(B-9).

If $n = 2$, the surface is parabolic and

$$\overline{(1/\delta)} = \frac{1}{\delta_M - \delta_m} \ln \frac{\delta_M}{\delta_m} \tag{B-15}$$

$$h_i = h_{iu} \frac{\delta M + \delta m}{2(\delta_M - \delta_m)} \ln \frac{\delta M}{\delta_m} \tag{B-16}$$

Let $\delta_M = C\ \delta_m$, then Eq(A2-16) becomes

$$h_i = h_{iu} \frac{C+1}{2(C-1)} \ln C \tag{B-17}$$

Eq(B-17) is unbounded as $C \to \infty$ because the film becomws vanishingly thin near the center of the bottom of the droplet. Eq(A2-17) is plotted in Figure B-2 for $C = 2$, 10 and 50.

Large values of n and C correspond to a thin film that tends to spread out and coat the sides of the bubble. For large values of n, Eq(13-13) can be approximated by

$$\overline{(1/\delta)}_{n>>1} \approx \frac{1}{\delta_m} \left(\frac{1}{C}\right)^{1/n} \tag{B-18}$$

and Eq(A2-12) becomes

$$h_i = h_{iu}\left[1 + \frac{2C}{n}\right] \left(\frac{1}{C}\right)^{2/n} \tag{B-19}$$

Note that this result is conservative since heat transfer through the film coating the side of the bubble has been neglected. Eq(B-19) also appears in Figure B-2 for $n = 40$ and $C = 50$.

B.2 Convection Models

There is considerable experimental evidence indicating that the dispersed phase liquid in an evaporating droplet is not stagnant. Shear stresses on the surface of the droplet induce internal circulation and vortex shedding in the wake can result in shape oscillations and erratic motion of the droplet. Hughes and Gilliland [23] observed oscillation induced eddies in the droplet, while Spangenberg and Rowland [24] reported the existence of thermal currents. Calderbank and Korchinksi [25] reported that drop oscillations can reduce internal phase resistance by from 7 to 71 compared to pure conduction.

Although there are numerous correlations for convective heat transfer in flow past cylinders, spheres, flat plates and packed beds, there is very little in the literature concerning convective heat transfer within an evaporating droplet. Therefore, it is necessary to exercise some judgement in the application of correlations to this process.

Despite Nazir's [10] assertion that the liquid inside the droplet effectively coats the entire interior surface, there is still convincing evidence that most of the liquid resides in the bottom of the droplet. Klipstein's [16] data had the same Re dependence as data for flow over cylinders in which most of the heat transfer occurred in the turbulent wake, which suggests that the heat transfer is primarily through a turbulent wake to the dispersed phase liquid in the bottom of the droplet.

Although circulation within the droplet tends to reduce skin friction, delay boundary layer separation and promote potential flow from the forward stagnation point to the point of separation, in the wake region surface rippling and skin friction tend to agitate the liquid inside the droplet and induce turbulence and the eddy diffusion observed by Hughes and Gilliland [23]. Consequently, the value of Re may not imply turbulent behavior, since the heat transfer probably occurs primarily in the wake. It is, however, necessary to use a correlation with a turbuelnt Re dependence.

Handlos and Baron [26] derived such a correlation for the liquid film inside a droplet

$$Nu = .00375\ Re_f\ Pr_f/(1 + \mu_d/\mu_c) \qquad \text{(B-20)}$$

When the appropriate constraints are substituted into Eq(B-20) the result is

$$h_i = 0.8\ r^{1/2}\ \frac{kw}{m^2\,^oK} \qquad \text{(B-21)}$$

Eq(B-21) also appears in Figure B-2. Comparing the conduction and convection results suggests that the constant in the Handlos-Baron correlation is too low. This is not surprising since Eq(B-20) was derived for pure liquid droplets not evaporating droplets. Similarly, although the correlation for the external heat transfer coefficient for cylinders and evaporating droplets both follow the same general form

$$Nu = 2 + c\ Re^{0.9}\ Pr^{1/3} \qquad \text{(B-22)}$$

the value of c is .016 for cylinders and .096 for evaporating droplets. If the value of the constant in Eq(B-20) is increased by a factor of six, the result is

$$h_i = 4.8\ r^{1/2}\ \frac{kW}{m^2\,^oK} \qquad \text{(B-23)}$$

Eq(B-23) also appears in Figure B-2, and for small values of r it is between 7 and 71 times as large as the pure conduction heat transfer coefficients as Calderbank and Korchinski [25] reported.

B.3 Conclusion

For small values of r ($r < 4$ and $x_v < 30\%$) turbulence in the liquid film will result in an internal heat transfer coefficient several times larger than the overall value. For $r > 4$ even the conservative assumption of pure conduction results in an internal heat transfer coefficient much larger than the overall value. Consequently, even for a dispersed phase (butane) with a thermal conductivity five times smaller than the continuous phase (water), there appears to be sufficient justification for neglecting the internal heat transfer resistance. Nevertheless, the details of the process are of enough importance to warrant further investigation.

TABLE B.1

THE THERMOPHYSICAL PROPERTIES
OF BUTANE AND WATER

Property	Units	Butane	Water
ρ_l	kg/m^3	600	1000
ρ_v	kg/m^3	2.78	
μ	kg/ms	.00202	.00155
K	KJ/msK	.0001072	.00056
C_p	KJ/kgK	2.26	4.186
L_d	KJ/kg	385	

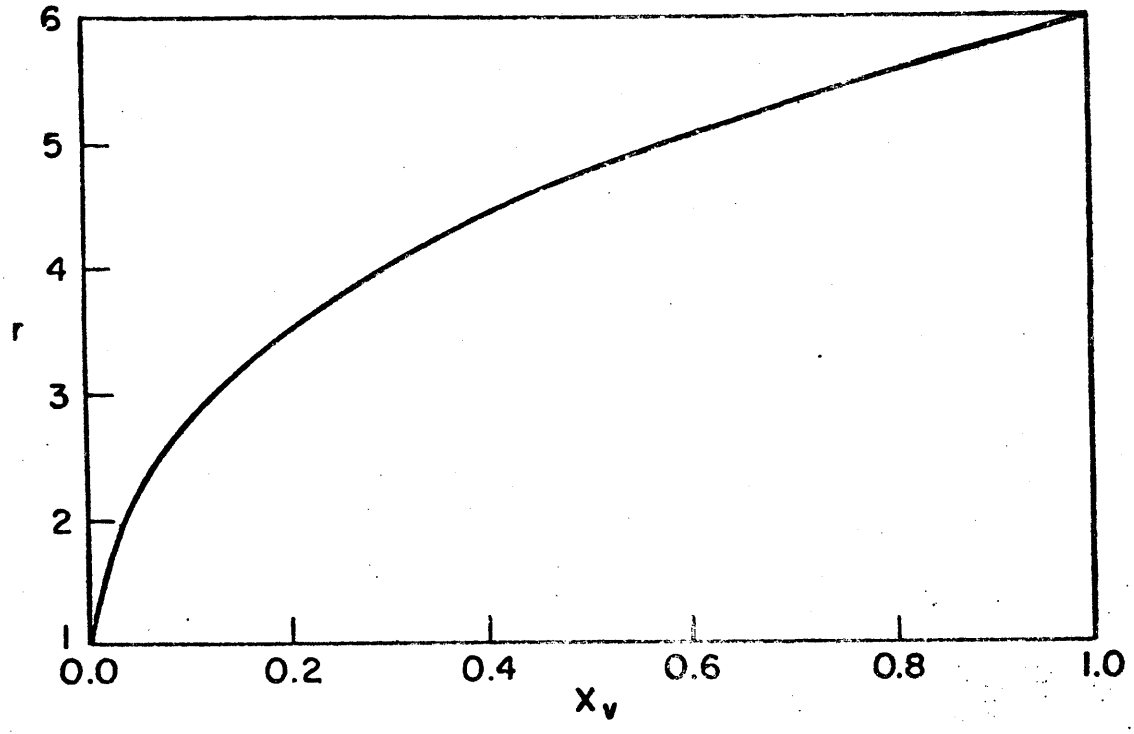

Figure B-1. Vapor Mass Fraction vs.
Equivalent Spherical Diameter Ratio

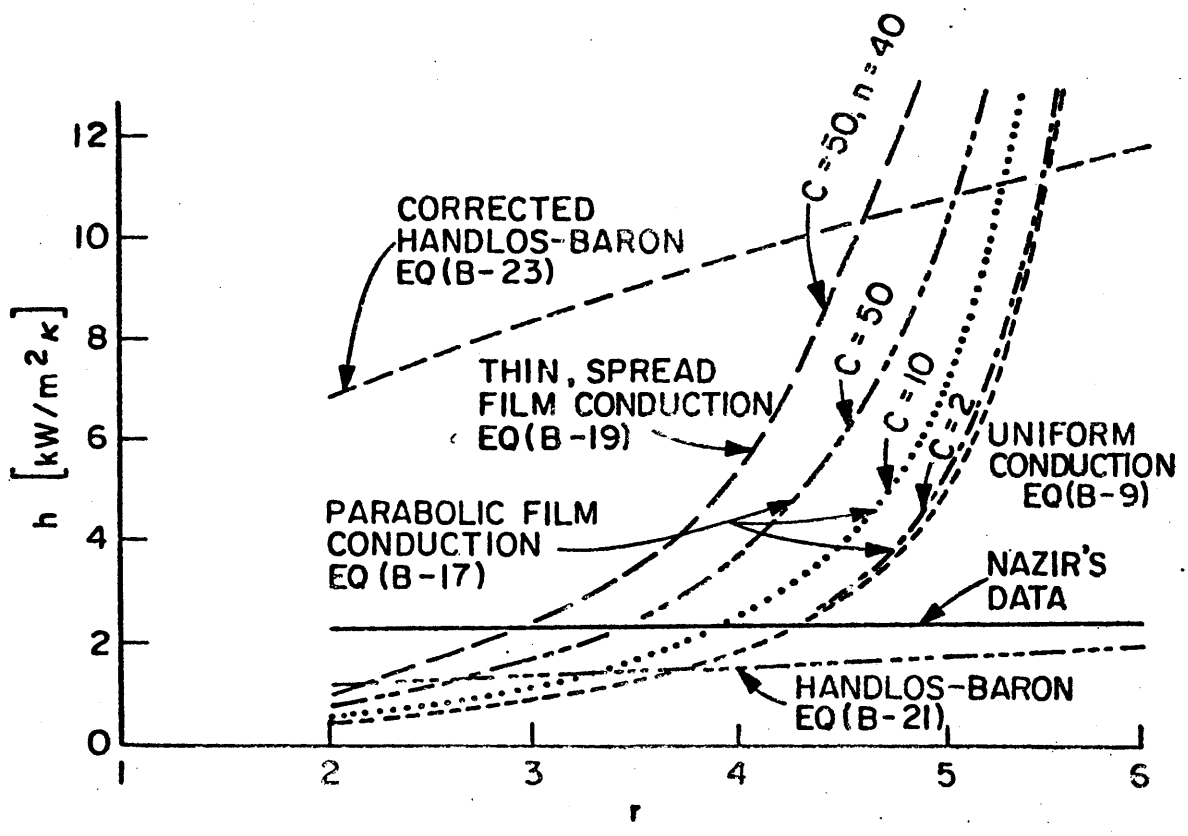

Figure B-2. Comparison of Internal and Overall Heat Transfer Coefficients for Butane Droplets Evaporating in Water

REFERENCES

1. Jackson, J. F. and Ostensen, R. W., "Mechanical Disassembly of FFTF Reactor," Argonne National Laboratory Intra-laboratory memo (October 1973).

2. Smith, L. L. et al., "SIMMER-II: A Computer Program for LMFBR Disrupted Core Analysis," Los Alamos Scientific Laboratory report LA-7515-M NUREG/CR-0453 (1978).

3. Wallis, G. B., One-dimensional Two-phase Flow, McGraw-Hill, New York (1969).

4. Batchelor, G. K., An Introduction to Fluid Dynamics, Cambridge University Press, Cambridge, England, p. 407 (1970).

5. Rohsenow, W. M. and Choi, H., Heat, Mass and Momentum Transfer, Prentice-Hall, Englewood Cliffs, New Jersey (1961).

6. Hadamard, J. M., "Mouvement permament lent d'une sphére liquide et visqueuse dans un liquide visqueux," Compt. Rend. Acad. Sci., 152 pp. 1735-1738.

7. Rybczinski, W., Bull. Acad. Aci. Cracovie, 1911, A40.

8. Garner, F. H. and Grafton, R. W., "Mass Transfer in Fluid Flow from a Solid Sphere," Proceedings of the Royal Society, A224 pp. 64-82 (1954).

9. Linton, M. and Sutherland, K. L., "Transfer from a Sphere into a Fluid in Laminar Flow," Chemical Engineering Science 12, pp. 214-219, (1960).

10. Simpson, H. C., Beggs, G. C. and Nazir, M., "Evaporation of a Droplet Rising through a Second Immiscible Liquid: A New Theory of the Heat Transfer Process," Heat Transfer, Vol. 5, Paper CT2.3 (1974).

11. Davies, R. M. and Taylor, G., "The Mechanics of Large Bubbles Rising through Extended Liquids and through Liquids in Tubes," Royal Society Proceedings, A200, pp. 375-390 (1950).

12. Haberman, W. L. and Morton, R. K., "An Experimental Study of Bubbles Moving in Liquids," Transactions of the American Institute of Civil Engineers, 121, pp. 227-252 (1956).

References (Cont'd)

13. Rosenberg, B., Taylor Model Basin Report 727, U.S. Navy Dept., (1950).

14. Levich, V. G., Physico-Chemical Hydrodynamics, Prentice-Hall (1962).

15. Sideman, S. and Taitel, Y., "Direct-Contact Heat Transfer with Change of Phase: Evaporation of Drops in an Immiscible Liquid Medium," International Journal of Heat and Mass Transfer, Vol. 7, pp. 1273-1288 (1964).

16. Klipstein, D. H., "Heat Transfer to a Vaporizing Drop," D. Sc. Thesis M.I.T. Cambridge, Massachusetts (1963).

17. Fair, J. R., Lambright, A. J. and Anderson, J. W., Ind. Engineering Chemical Process Design Development, 1, 33 (1962).

18. Kazimi, M. S. and Chen, J. C., "Void Distribution in Boiling Pools with Internal Heat Generation," Nuclear Science and Engineering, 65 pp. 17-27 (1978).

19. Sideman, S. and Gat., Y., "Direct Contact Heat Transfer with Change of Phase: Spray-Column Studies of a Three-Phase Heat Exchanger," American Institute of Chemical Engineering Journal, pp. 296-303 (March 1966).

20. Bordley, P., "Photographic Study of Bubbles in a Direct-Contact Boiler," B.S. Thesis M.I.T. Cambridge, Massachusetts (1980).

21. Henninger, R. J. and Alcouffe, R. E., "Disassembly Phase Energetics: An Examination of the Impact of SIMMER Models and Assumptions," Los Alamos Scientific Laboratory informal report LA-7998-MS NUREG/CR-1027 (1979).

22. Mori, Y. H., "Configurations of Gas-Liquid Two-Phase Bubbles in Immiscible Liquid Media," International Journal of Multiphase Flow, 4, pp. 383-396 (1978).

23. Hughes, R. R. and Gilliland, E. R., "The Mechanics of Drops," Chemical Engineering Progress, 48, p. 497 (1952).

24. Spangenberg, W. G. and Rowland, W. R., "Convective Circulation in Water Induced by Evaporative Cooling," Physics of Fluids, 4, p. 743 (1961).

25. Calderbank, R. H. and Korchinski, I. J. O., "Circulation in Liquid Drops," Chemical Engineering Science, 6 p. 65 (1956).

26. Handlos, A. E. and Baron, T., "Mass and Heat Transfer from Drops in Liquid-Liquid Extraction," American Institute of Chemical Engineers Journal, 3 p. 127 (1957).